Position and Strain Feedback Control for Shaping an Active Truss

by

Lawrence B. Tentor

Thesis submitted to the Faculty of the

Virginia Polytechnic Institute and State University

in partial fulfillment of the requirements for the degree of

MASTER OF SCIENCE

in Mechanical Engineering

APPROVED:

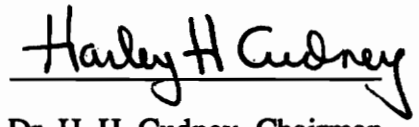

Dr. H. H. Cudney, Chairman

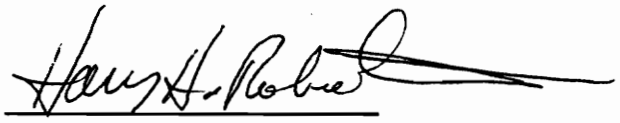

Dr. H. H. Robertshaw

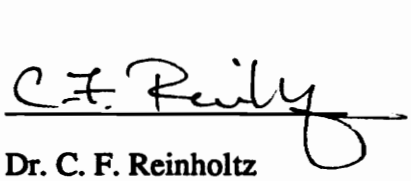

Dr. C. F. Reinholtz

May 1993

Blacksburg, Virginia

POSITION AND STRAIN FEEDBACK CONTROL FOR SHAPING AN ACTIVE TRUSS

by

Lawrence B. Tentor

Committee Chair: Harley H. Cudney

Mechanical Engineering Department

Virginia Polytechnic Institute and State University

(ABSTRACT)

The design requirements for future aircraft demand increased performance and multi-mission capability. Active, in-flight, aerodynamic surface shaping is currently being investigated to increase the flight envelope of tomorrow's aircraft. The primary application of this research is to aid the evaluation of active airfoil and wing shape control using an active truss. This specific research addresses the effect of replacing position feedback with strain feedback for shape control of an active truss. There are two research objectives: a comparison of multiple beam shape control using position and strain feedback, and to confirm a system displacement model through experimentation.

The experimental setup uses two cantilevered aluminum T-sections attached by one to three ball screw actuators. The actuators have been pinned at each beam location to allow rotation during extension, while also allowing the effect of a variable number of actuators to be examined. The three-actuator arrangement enables independent specification of three positions along the two beams; therefore, the system is a multiple input-multiple output (MIMO) system. The controller consists of three pulse-width modulated amplifiers converted for use with a position feedback loop. A model is developed which consists of a spring-actuator arrangement with the equivalent spring constants corresponding to the beam deflection equations.

The system model is first examined based on the results of the actuator length feedback experiments. The model is confirmed for the single actuator system. The joint gap accounts for the inconclusive results in confirming the multiple actuator displacement model. The next set of experiments demonstrate that strain feedback may indeed replace the actuator length feedback. It is shown that a signal may be produced which is proportional to the actuator extension, this may then replace the length sensor.

Acknowledgments

This research is the culmination of the efforts and motivation of many people. Primarily I thank Dr. Harley Cudney for being my advisor, committee chairman, mentor, and friend. I recognize that, at times, I have been a challenge with which to work. I thank him for his guidance, support, and understanding. I would also like to acknowledge Dr. Harry Robertshaw and Dr. Charles Reinholtz for serving on my committee. I also thank Dr. Al Wicks for his guidance on data analysis of experimental work.

I also thank Grumman Aerospace of their initial guidance and help on this project. Mr. Mike Rossi, Mr. M. Kesselman and Dr. Gareth Knowles had helped with the supervision and direction of my initial efforts.

I am also indebted to my co-workers and friends in the laboratory, especially for the support, motivation, and encouragement received from John Richard, John Finefield, Christina LaPeter, Rich Lomenzo, Joe Colvin, Chris Niezrecki, Greg Diehl and Anton Sumali.

I thank my parents for all their support and guidance they have given me, at times when I wanted it and even those times I didn't ask. I thank many friends which helped motivate, inspire, and prod me on. These include, Catherine Traffanstedt, Ananta Hejeebu, Tim Lilley, Matt Robertson, and Miché Young.

Table of Contents

Chapter 3: System Modeling

4. Experiment Results and Discussion

5. Conclusions and Recommendations

List of Figures

List of Tables

Nomenclature

Parameters

A	Amplifier Gain Characteristic
A_i	i^{th} position along beam A
A_{ij}	i^{th} to j^{th} actuator mounting location
B	Flexibility Matrix
Bij	Flexibility Matrix Elements
Bi	i^{th} position along beam B
C_f	Fixed Compensator Capacitance (0.047 μF)
C_i	Fixed Compensator Capacitance (0.022 μF)
D	Motor Viscous Damping Factor
E	Modulus of Elasticity
$\mathbf{E_3}$	Linear Transformation from Point Displacements to Actuator Extensions
F_n^{AT}	Transverse Force on Beam A at Position n
F_n^{BT}	Transverse Force on Beam B at Position n
g_i	i^{th} Strain Gage Gain
G	Gain Matrix
G_a	Amplifier Voltage Gain
G_r	Reference Signal Gain
G_p	Position Feedback Gain
I, I_{ZZ}	Area Moment of Inertia
J	Scaling Value for Normalized Gain Matrix
J	Motor Armature Inertia
K_{BS}	Ball Screw Gearing Constant

K_e	Motor back EMF constant
K_i	Amplifier Current Gain
K_p	Position Feedback Gain
K_s	Load Spring Constant
K_t	Motor Torque Constant
Kv	Amplifier Voltage Gain
K_i	Lumped Parameter Spring Constants
L	Inductance
L	Distance Matrix
L_a	Motor Armature Inductance
L_n	Distance of Point n from Cantilever End
M_n^A, M_n^B	Moment on Beams at Point n
n	Gear Ratio
R	Resistance
R_a	Armature Resistance
R_{il}, R_{fl}	Adjustable Compensator Resistance, 5-100 KΩ
R_{i2}	Fixed Compensator Resistance = 100 KΩ
R_{f2}	Fixed Compensator Resistance = 10 MΩ
S_i	i^{th} strain gage mounting locations
T	Torque
V_ε	Voltage from Bending Strain
V_{motor}	Motor Voltage
V_{out}	Compensator output voltage
V_{in}	Compensator input voltage
x	Distance between Actuator Attachment Points
X	Displacement of Actuator

y	Distance that strain gages are mounted from neutral axis
y	Distance between beams
Δy	Change in distance between beams
Y^A	Displacement of beam A
Y^B	Displacement of beam B

Greek

δ	Actuator Undeformed Length
$\Delta\delta$	Actuator Extension
τ_a	Electrical Time Constant
ω	Motor Shaft Speed
Θ	Motor Shaft Angle

Operators

$< >$	Singularity functions
s	LaPlace Operator

Chapter One
Introduction

1.1 Motivation

Airfoil selection and control surface placement directly affects aircraft control performance. Flight control is achieved by changing the wing camber and control surface orientation. This change in camber provides varying aerodynamic pressures that direct the flight path. This is traditionally accomplished using flaps, ailerons, and rudders. These alternatives leave parameters such as the leading edge shape, the airfoil internal chord profile, and the aileron, flap and rudder shape fixed. Rigid body control surface motion has been the standard approach for aerodynamic control. Since this approach leaves the internal chord contour fixed, which then creates airfoil curvature discontinuities, it increases the drag, thereby limiting performance. Active airfoil shaping is a potential way to address these issues.

New aircraft are being developed to satisfy multi-mission demands. These aircraft have performance specifications for both low and high speed flight. Low speed aircraft loiter provides longer time aloft for radar surveillance missions, while high speed dash is important for penetration missions. Since loiter conditions tend toward one airfoil selection and dash conditions tend to emphasize other airfoil features, designers traditionally select a compromised airfoil cross section suitable for all conditions. Given the performance requirements specifying a larger flight envelope, designers are seeking innovative approaches.

Several performance enhancing features have been previously investigated. The F-14 configuration has swing wings. A swing wing enables skewed airfoil profiles to be used rather than simply a fixed wing approach. This solution allows a limited family of airfoil shapes to be implemented, while also altering the wingspan dimension.

Various researchers have investigated aerodynamic surface contouring. The AFTI/F-111 Mission Adaptive Wing (MAW) was a configuration implemented to allow leading and trailing edge contouring. Performance was tracked over various flight conditions of loiter, penetration, cruise, and maneuver. Notable enhancements were obtained in both cruise and maneuver conditions (Bonnema and Lokos, 1989).

The current investigation is focused on airfoil contouring between the leading and trailing edge control surfaces. Figure 1.1.1 shows how a proposed system was simplified into a suitable test-bed. A cross section of the wing is taken at a supporting frame location. The elements of this supporting frame are then made into active elements. Proper contouring of these surfaces will lead to aerodynamic performance gains. One design aspect is that the active truss structure must withstand an applied torque, as would a rigid wingbox. Two beams can represent a segment of the airfoil skin, while active lengths can replace selected ribs. This thesis concentrates on the modeling of shape control between two cantilevered beams with active lengths.

Shape control can also be used in large space structures. Low-weight, flexible space structures are difficult to construct to precise shapes, due to gravity and solar effects on orbit. To account for this, shape control is necessary. Example structures include large high-frequency, space-borne antennas that require their reflectors to be within a wavelength of a desired shape.

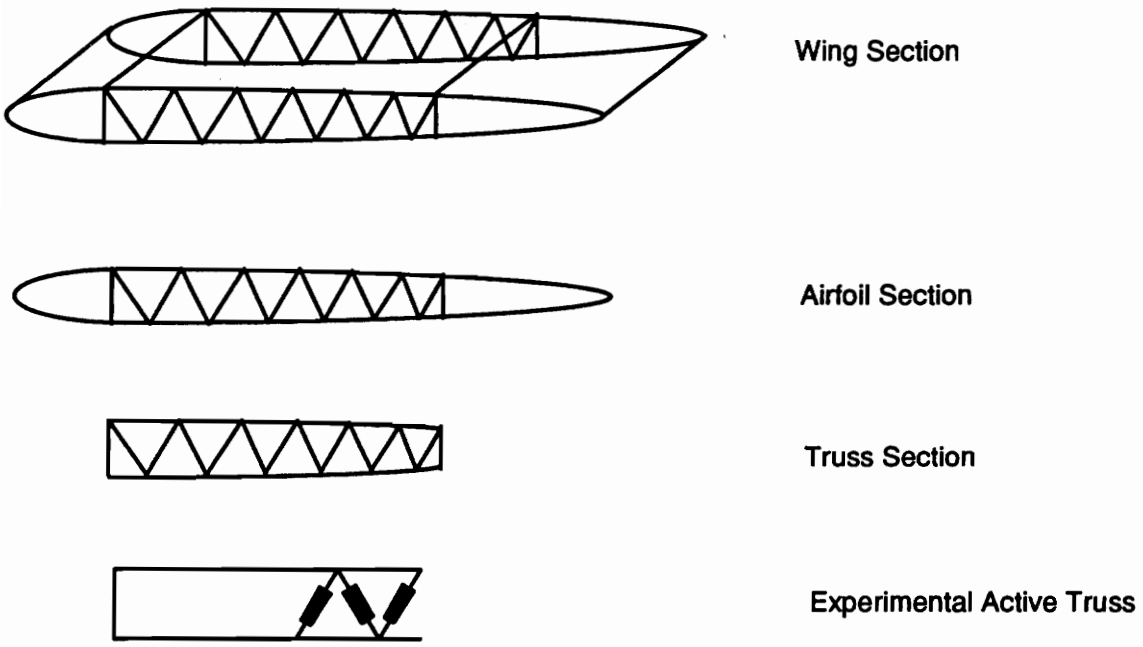

Figure 1.1.1: Model Simplification

1.2 Objective

The long term aspiration of which this work forms the basis is to produce a variable camber wing that alters its shape between 20%-80% of the chordline. As a first step, analysis of an active truss is examined. Figure 1.1.1 depicts the simplification of a wing section to an active truss. The first objective consists of developing a system model for two parallel beams connected by active members. This model will relate the actuator extensions to the beam displacements. The second objective is to examine the effect of replacing actuator position feedback with beam strain feedback while performing controlled beam deformation. This may allow the removal of heavy length sensors to be replaced with strain gages. The controlled displacements using the strain and extension feedback will be compared.

1.3 Approach

The approach of this research is as follows. First, the differential equations describing deformations will be formed. The model consists of the equations for the individual beams. The deformations of the active members may be used to evaluate the point forces at the attachment locations. The forces acting on the beam will have both transverse and axial components that are related to the structural geometry. Using the differential equations along with the kinematics of the actuators, a lumped parameter model will be developed. This model will describe the actuator attachment point displacement, beam strain, and actuator extension relationships.

The experimental setup uses two cantilevered aluminum T-sections attached by one to three active members. The actuators will be pinned to each beam to allow rotation during extension. This setup enables up to three independent positions along the two

beams to be specified. The control system consists of three pulse-width modulated controllers using both position and estimated velocity feedback. The reference input to the controller dictates the actuator extension. In the first set of experiments the Linear Variable Differential Transformer (LVDT) length signal is used as feedback into the controller. The second group of experiments demonstrates the use of strain measurements to predict actuator extensions.

1.4 Previous Work

The previous works applicable to this research are in the areas of shape control and adaptive structures. A number of sources have examined aerodynamic surface control, while others have applied shape control to various applications. Previous work is reviewed in this section.

There have been a number of studies relating directly to airfoil wing shaping. They cover initial phase research, laboratory experiments and flight test hardware. The best known project was the Advanced Fighter Technology Integration (AFTI) F-111 Mission Adaptive Wing (MAW) flight test. The motivation for this project was based on extending the operating range and increasing the efficiency of the aircraft. The project focused on increasing the aircraft aerodynamic efficiency during all phases of the flight envelope (Bonnema and Lokos, 1989). The program developed a variable camber wing and control system. The leading and trailing edges were made from flexible composite plates. These surfaces were contoured by electrohydraulic actuators. A smooth continuous upper surface allowed the MAW to accomplish the shape control without the increased drag associated with discontinuities.

Twenty-six flights were performed with manual pilot control of the adaptive wing; while another battery of tests were run with the automatic control system. Four automatic modes were available with the flight control system. These four modes addressed the different flight conditions of: Maneuver Camber Control, Maneuver Load Control, Cruise Camber Control, and Maneuver Enhancement and Gust Alleviation.

This program had the F-111 aircraft specially instrumented to record air data, engine parameters, accelerometer data, and structural loads. A wing deflection measurement system was implemented to examine in-flight effects of the variable camber wing. Overall the program demonstrated that performance improvements can be achieved with a practical wing system that varies its contour in flight, either by manual or automatic control.

A second study investigated compliant wing sections for adaptive control surfaces (MacLean, *et al.* 1991). This study used integrated structural actuators to provide controlled curvature. Embedded shape memory wires were used as actuators. To hold a specified position the alloy temperature must remain constant. This is done by applying an electric current to balance the environmental cooling. The study focused on the power necessary to hold the wing section at the commanded deflections and examining the deflection rate and power relation. The work demonstrated the ability to control a winglet panel section with shape memory alloys.

An additional study by Turner (1991) focused on actuated wing spars. The focus was on distributed sensors and actuators for health monitoring and shape control of wings. Each wing model had a forward and rear spar for bending and torsion control. Each spar had eight piezoelectric sensors with sixteen piezoelectric actuators to act as an active beam. By using various actuators a wing could take on different local dihedral angles. This

arrangement allowed a change in the spanwise wing configuration. This thesis takes a different approach by examining chordwise profile changes.

The above work focuses on aerodynamics applications of adaptive structures. Other work on shape control has been directed towards large space structures. Shape control has been developed in the optics and space community since the late 1960's.

The optics community has sought to have wavelength precision mirrors which require active elements due to manufacturing imprecision and mass loading. Padula, *et al.*, (1989) developed a procedure for reflector static shape control. This procedure accounted for structural design, shape control and electromagnetic performance as dependent issues. They present possible compensations for electromagnetic performance using shape control. Using another approach, Lang (1982) explored using distributed electrostatic forces for shape contouring of a thin member. Kashiwase, *et al.* (1991) experimented with shape control of an aluminum plate with sixteen pairs of discrete sensors and actuators.

A number of studies have been done with adaptive trusses. The work encompasses design, kinematics, modeling, and control issues. These trusses come in both planar and three-dimensional variations. A variable geometry truss (VGT) is a statically determinate truss that has been modified to contain a number of variable length members (Padmanabhan, 1990). These trusses have found application in robotic manipulator problems. The current work is different from the above primarily because the structure is indeterminate and contains elastic members.

Kuwao, *et al.* (1989) examined the mathematical models for vibration and shape control of an adaptive truss structure. This model has thirty-six actuators occupying diagonal

members of a cubic structure. They evaluated a method of shape compensation for gravity loading using prescribed truss member extensions. Their work could also be applied to the quasi-static thermal distortion problem.

Bushell (1979) examined shell surface configuration control using applied forces. His work focused on correction of telescopic mirrors. Bushell defined the difference between a displacement actuator, a device that is stiff compared to the structure; and a force actuator, a non-rigid device that generates force commands. Bushell's work implemented force actuator models. The major difference in this thesis is that displacement actuators are used.

Chen and Zhou (1990) examined boundary element methods for distributed parameter systems. They applied their modeling to shape control of a Timoshenko plate. A round elastic rubber plate with a finite number of sensors was controlled by using bending and shearing forces at the boundary. They demonstrated how boundary element modeling and boundary control can be applied to shape control problems.

This thesis addresses shape control of two cantilevered beams representing a truss in a wing section. The chordwise profile changes will be examined. Displacement actuators are used to control the shape. This work uses an indeterminate structure. Herein is presented a lumped parameter model to facilitate understanding of two-dimensional airfoil control. From this lumped parameter model the beam shape can be derived. This is different from variable geometry trusses in that the structure studied has elastic components that are being shaped.

1.5 Overview & Organization

The presentation of the research is outlined as follows. In Chapter 2 the experimental apparatus, including the beams, actuators, sensors and amplifiers are described. In Chapter 3 the approach used to model the system is outlined. The experiments performed and a discussion of the results are presented in Chapter 4. Conclusions and recommendations for further research in this area are made in Chapter 5.

Chapter Two
Experimental Apparatus

2.1 Introduction

This chapter describes the test-bed arrangement and how it pertains to accomplishing the research objective. The component selection is explained for the structure, actuators, sensors, and amplifiers. The descriptions are included to understand the system modeling undertaken in Chapter 3.

2.2 Experimental Design

The goal of this work is to examine shape control using an elastic truss structure. First the simplified experimental test-bed is designed. Then the entire system is modeled. The test-bed is chosen to examine shape control using active truss members. One important aspect is the type of feedback signal used to measure the actuator lengths because it impacts the size, weight, measurement type, and system stability. This work examines both the LVDT extension signal and the beam strain gage output.

2.3 Description of the Structure

The structure used for this experiment is selected to control beam shape control while minimizing the test-bed complexity. The primary consideration is that the structure must alter its shape under normal actuator loads. It is also important that the beams remain in the elastic deformation region and do not plastically deform.

To fulfill this design two cantilevered T-sections are mounted 127 mm above a base platform. The T-sections are extruded 6063-T52 aluminum configured to have a reasonable displacement to stiffness relations within the elastic range. Figure 2.3.1 is a picture of the test-bed. The fixed end condition replicates how the wing skin attaches to the leading and trailing edge. In this case, three bolts have been placed 12.7 mm apart to restrain displacement and rotation at the root. At the other end, the free end conditions enables deflections with minimum strain, and avoids nonlinear geometric stress stiffening due to constraints at both ends. The distance between the root and the free end is 559 mm. Thus, the beam cantilevered boundary conditions were selected to replicate the attachment point and allow sizable deflections near the free end.

The T-section was chosen for two reasons. First, it allows an easy connection point for the active lengths. Secondly, the force necessary to provide elastic deflections remains within the actuator specifications. The T-member is 19. mm x 19. mm and is 3.18 mm thick. The cross section area moment about the centroid is 3603.3 mm^4. The maximum transverse force while in the elastic range is 307 N at 127 mm from the root. The associated displacement is only 0.838 mm. At 533 mm from the root a 76 N force provides a 15.2 mm maximum elastic deflection. A peak wing defection of 2-3% of chord is expected to alter aerodynamics performance. Along this entire beam a 2.8% change is attainable while the beams are still in their elastic range.

The two beams are connected by active members. These active lengths and elastic beam segments constitute an adaptive truss. Each variable length segment consists of an active member and a position sensor. These components are mounted together using a bracket.

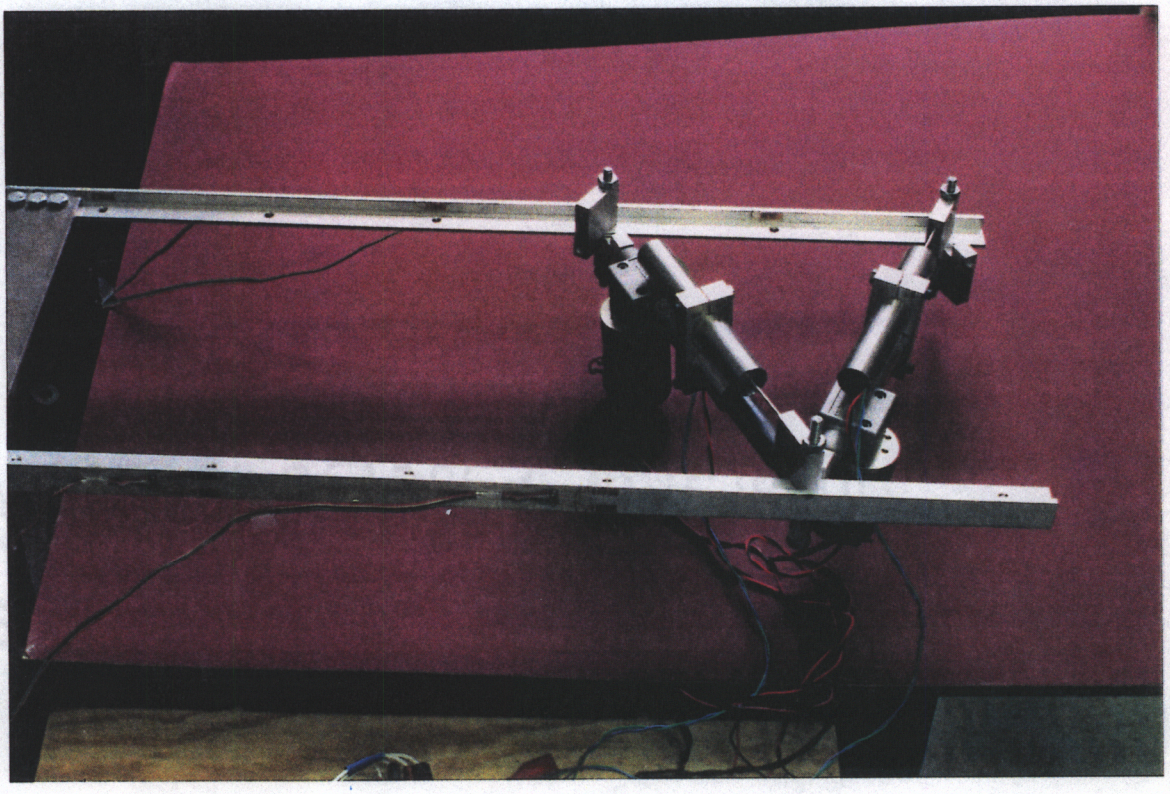

Figure 2.3.1: System Photograph

This arrangement allows the actuator to act as a controllable length member. Since a wing box must sustain a torsional wing loading, this truss must also handle this condition. For this reason the actuators are oriented in a truss-like manner, this is shown is Fig. 2.3.2a. Figure 2.3.2b depicts a configuration that will pivot as a mechanism, which is unacceptable. Figure 2.3.3 shows a picture of the actuator and sensor pair. Half-clevises were constructed to enable pinned-pinned end conditions for attachment to the T-sections. This allows a moment release for the actuators as they are extended. Therefore, the actuator lengths only sustain axial loads. The half-clevises allow two actuators to be positioned at coincident locations. With this type of connection, the T-section will be subjected to transverse and axial loads. The nomenclature for various component locations are shown in Fig. 2.3.4. Five mounting locations were built and are accessible.

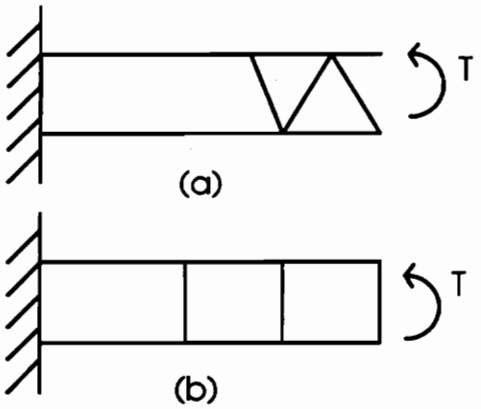

Figure 2.3.2: Torsional Loading of Two Configurations

The components for the base and restraints are constructed of steel. The half-clevis and sensor-actuator bracket used between the beams are aluminum. This is to keep the suspended weight between the T-sections low. The sensor-actuator attachment bracket allows the sensor to slide such that an electronic zero position may be calibrated.

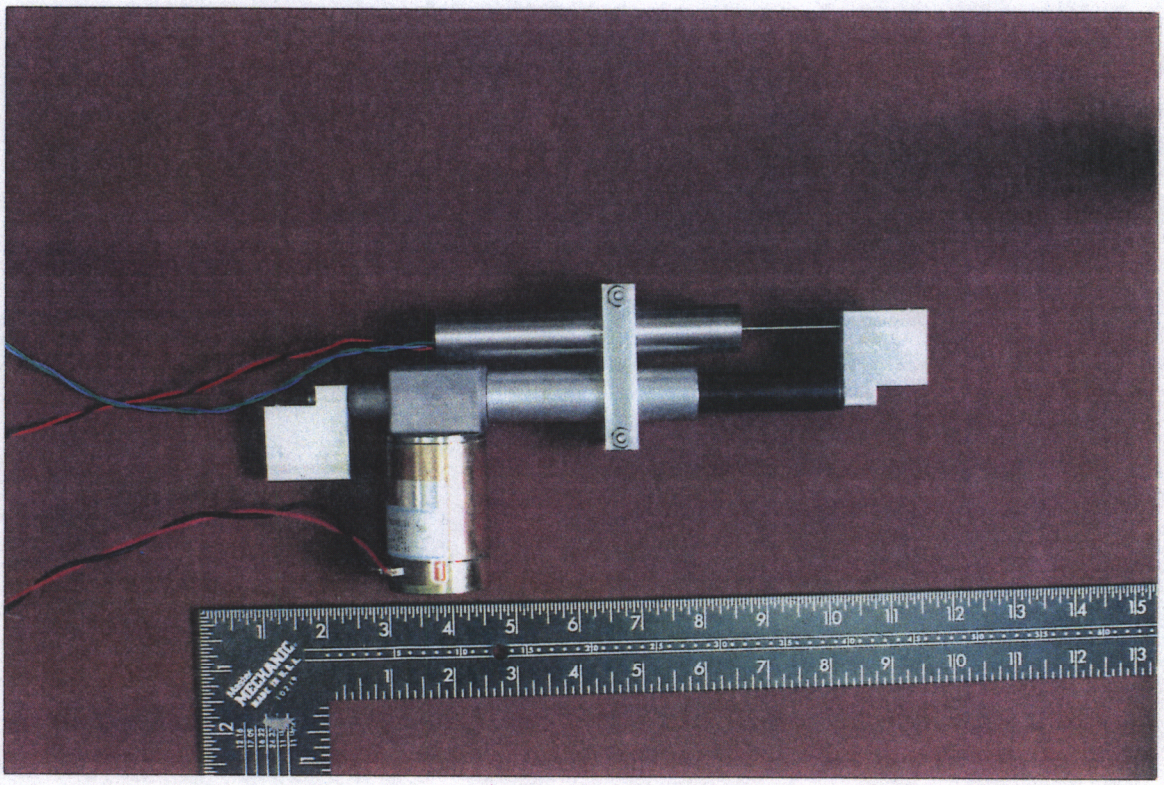

Figure 2.3.3: Actuator and Sensor Pair

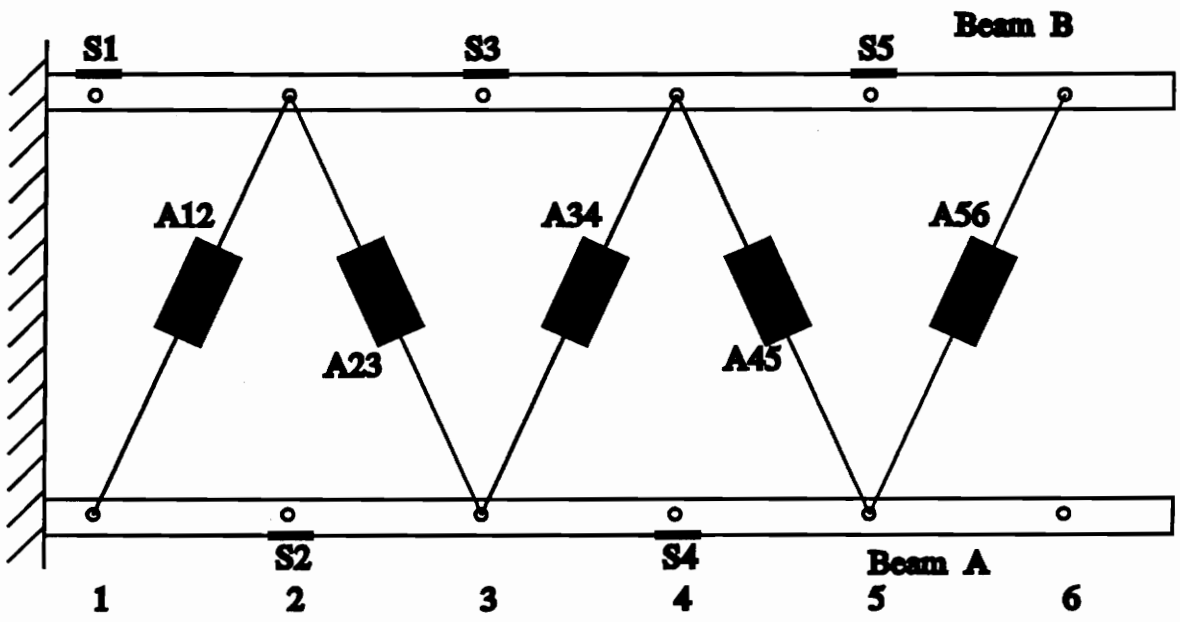

Figure 2.3.4: Experiment Schematic

The clevises are designed to allow two actuators to connect to the same attachment point. These clevises require a 35 degree angular separation. The unstrained initial configuration has 49 degrees of angular separation available. This allows ample shifting and twisting during extension to prevent jamming. By design, the minimum angle between the actuator and the T-section is 47 degrees. Therefore each actuator has a 25 degree rotational freedom.

The beam deflections are measured in relation to a fixed datum wire. These wires are positioned parallel to each undeformed beam.

2.4 Actuator Characteristics

The primary experimental focus is static shape control. An actuator is needed to provide transverse beam deflections. With this in mind, the response time of the actuator is not a primary concern, yet does affect the control modeling. The main concerns are the system stability and the static force which can be maintained. A secondary consideration is a measurable displacement within the elastic region. The power supply components must be chosen based on the selected actuators. Although weight is a driving factor within the aerospace industry, in this demonstration article weight constraints have been neglected.

From the above criteria, the actuator chosen is an electromechanical ball-screw type. It has an epicyclic ball screw with integral freewheeling at the stroke ends, thereby eliminating the need for limit switches. The maximum stroke is 50.8 mm. The actuator selected is short relative to the allowable displacement. The overall retracted length of

the actuator is 170 mm before the clevises are secured. The minimum length with the clevises, which can be lengthened based on the stud selection, is 226 mm. This allows a full extension of 277 mm. The maximum dynamic axial load is 445 N. A static load of up to 2670 N can be restrained.

The motor input is ± 24 volts. This allows maximum motor speeds of up to 7500 rev/min. Under these conditions the no-load stroke speed is found to be 12.7 mm/sec with the selected gear reduction. The actuator and motor specifications are listed in Table 2.4.1.

2.5 Sensor Description

Sensors are required to monitor the experimental state. In order to control the actuator length a feedback sensor is required. A position sensor is chosen to accurately monitor the actual length. A linear position sensor mounted in parallel with the actuator will transduce the actuator displacement. The sensor selection criteria dictated that it be shorter than the actuator, maintain acceptable accuracy, and allow easy mounting to the actuator.

A series 240 Trans-Tek DC-DC displacement transducer was selected. It is a linear variable differential transformer (LVDT) with solid state oscillator, and a phase-sensitive demodulator. The transducer has infinite resolution and high sensitivity. There is no inherent hysteresis within the transducer. The LVDT has two input supply wires for 6 to 30 volts. The output is a voltage proportional to the axially core displacement. This

sensor is used in a servo position feedback arrangement. Table 2.5.1 summarizes the LVDT features.

Table 2.4.1: Ball Drive Actuator Specifications

Manufacturer	Motion Systems Corp.
Model Number	85615
Motor Voltage	24 Volts
Maximum RPM	7500 Rev/min
Load capacity	445 N dynamic
	2670 N static
Stroke	51 mm
Gear Ratio, n	30:1
Lead Screw Ratio	0.315:1 rev/mm
No Load Stroke Speed	12.7 mm/sec
100 lbf Load Stroke Speed	10.2 mm/sec
Armature Resistance, R_a	2.12 Ohm
Armature Inductance, L_a	1.56 mH
Motor Inertia, J	$4.2 * 10^{-6}$ m N s^2
Motor Damping, D	$2.6 * 10^{-6}$ m N/(rad/s)

Table 2.5.1: LVDT Transducer Characteristics

Working Range	± 25.4 mm
Maximum Range	± 25.4 mm
Minimum Input Voltage	6 Volts
Maximum Input Voltage	30 Volts
Linearity % of full scale	± 0.5%
Bandwidth	100 Hz
Output Impedance	5600 Ohm
Mass	108.3 g

In addition to the length sensors, the beam states can be estimated by measuring the strain. In order to monitor the strain, resistive gages are mounted along the beam. A comparison can be made between the actuator extensions and actual strain vs. predicted strain. In effect, the length sensors could be eliminated if a displacement/strain relation can be identified. The strain gage chosen is the Measurements Group, Inc. model CEA-13-062UW-350. It has a resistance of 350 Ohms. The gage factor is 2.160 ± 0.5%.

The strain gages are mounted and connected in a full bridge circuit such that the output is only sensitive to bending strain. In order to accomplish this, four axial gages are mounted at the same location along the beam, with two on the upper T surface and two on the underside. This enables a properly constructed bridge circuit to measure only bending strain. Although with this configuration on a T member the gage sensitivity factor is decreased proportional to the T-section thickness. The beam configuration is directly observable with the strain gages as long as there are no unmodeled loads.

2.6 Controller & Amplifier Selection

A controller and amplifier are required to alter the actuator lengths. A number of alternatives were considered. An analog controller is the simplest control method to implement. A linear amplifier circuit was examined, but would have to be constructed from components. For this reason commercially available amplifiers and motor controllers were examined.

A VXA series motor controller from PMI Motion Technologies was selected. This is a pulse width modulated (PWM) amplifier. The controller has one very nice feature in that it has a motor back electromotive force (EMF) estimation circuit. This feature enables an estimator to approximate the motor speed since this is directly proportional to the back EMF. Given this estimate and the position sensor output, the motor response can be nicely damped.

The amplifier was originally designed as a velocity servo device. It provides a jumper to select either tachometer feedback or EMF sensing. This experiment dictates altering the amplifier to work as a position servo. By defeating the jumper, both EMF sensing and an external feedback may be used. In this experiment the external input will be the position signal. The amplifier has a number of adjustments. It has a lag and lead adjustment for the control law. An adjustable input reference resistance allows control of the steady state output. A potentiometer also adjusts the position input level. It also has a current limiting circuit to adjust the maximum continuous amperage output. Other controller specifications are listed in Table 2.6.1.

The amplifier also has a jumper for torque or speed control. While using the analog controller during this experiment, speed control will be selected. If the speed compensator is not needed, as when another compensator is desired, the torque control may be selected so the component acts as straight amplifier. When using torque control no compensation is done to the input and the controller acts solely as a pulse width modulated current amplifier.

One transformer will supply three controllers with AC power input. The transformer can supply 20 V at up to 8 A. By restricting the current output of each amplifier through each motor to two amps this transformer is adequate.

Table 2.6.1: Motor Controller Characteristics

Maximum Output Voltage*	12-48 V AC
AC Input Voltage†	12-36 V AC
Continuous Current	8 A
Peak Current	8 A
Continuous Power Output	384 W
Switching Frequency	> 20 kHz
Bandwidth	1 kHz
Command Reference Signal	± 10 V DC

* Dependent on input

† 50 -60 Hz

2.7 Summary

This chapter has explained the experimental setup. It has elaborated on the characteristics of each component. The primary components which will be used consist of 3 LVDT displacement sensors, 3 ball screw actuators, 3 PMI controllers, 1 transformer, twenty strain gages and five channels of strain conditioners, 2 T-sections and the experiment base. These components will all be mounted on a test stand. The forthcoming chapter presents the component modeling.

Chapter Three
System Modeling

3.1 Introduction

The following sections contain the system mathematical models. This is the first step in providing shape control. Dynamic models of the actuator and the control amplifier are developed. These models are used to characterize the closed loop system dynamics. This model permits the design of a stable actuator length (LVDT) feedback and strain feedback system. Next, a static displacement model is developed. The physical system is viewed as a lumped parameter spring-actuator model. The predicted displacement will be compared with the measured displacements in the following chapter. Finally, the use of strain measurements in place of the actuator length signals is explored as a means to control the actuator displacements.

3.2 Modeling the Ball Screw Actuator

The actuator is a DC permanent-magnet motor connected with an epicyclic ball screw drive. This device acts as a component of a variable length member. The actuator is modeled as an armature-controlled direct current motor with a gear and lead screw reduction. An armature controlled DC motor and ball screw drive physical model with its block diagram representation is presented in Fig. 3.2.1. This depicts the relation from the input motor voltage to the output extension. The dashed items represents the effect of the structure on the actuator movement. A large gear ratio was desired for a high position accuracy and low velocity. Therefore, a 30:1 gear ratio was chosen. In

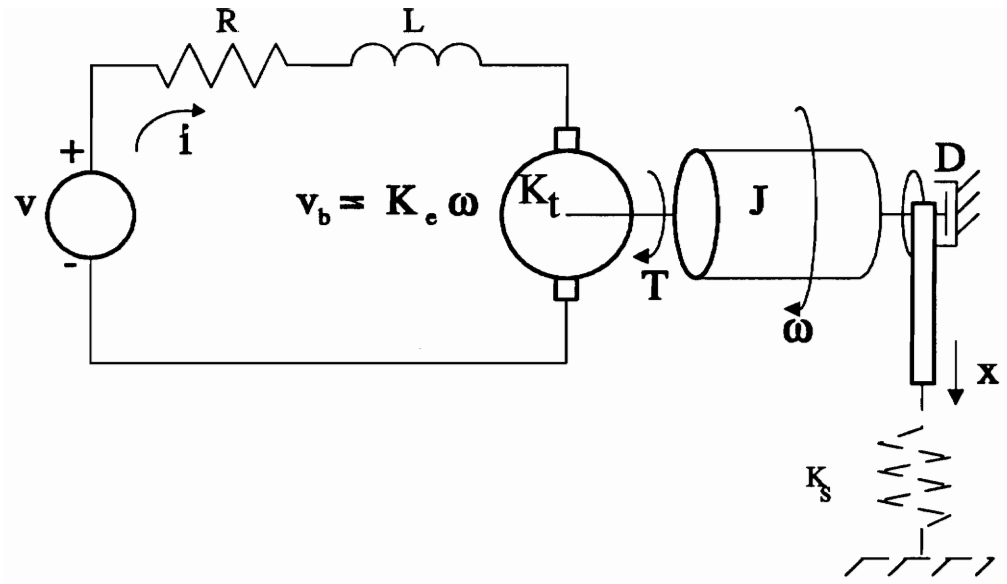

(a)

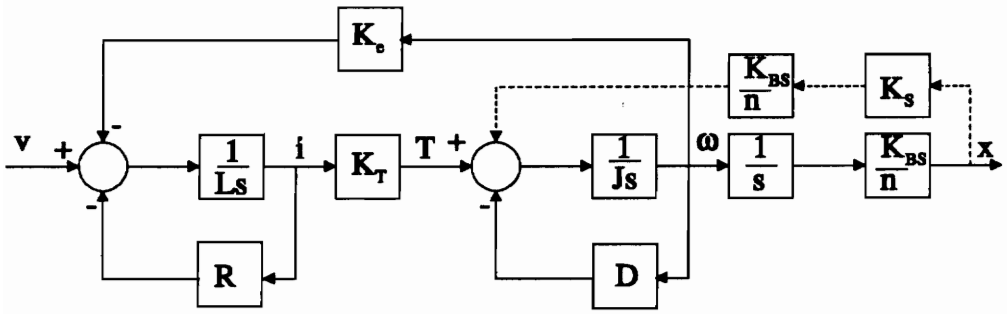

(b)

Figure 3.2.1: DC Motor and Ball Screw Model and Block Diagram

combination with this there is a 3.18 mm/rev ball screw lead. Therefore, the overall ratio of motor turns to actuator extension is 9.44 rev/mm.

The actuator is modeled as a linear system and the nonlinear phenomena of slop, gear backlash, and friction are not modeled. The block diagram analysis results in the following transfer function:

$$\frac{X}{V_{motor}} = \frac{K_T \cdot K_{BS} / n}{L_a J s^3 + (R_a J + D L_a) s^2 + (R_a D + (\frac{K_{BS}}{n})^2 K_s L_a + K_T K_e) s + (\frac{K_{BS}}{n})^2 R_a K_s}. \quad (3.2.1)$$

The actuator is found to be relatively insensitive to low external forces because of the friction and the high gear ratio, therefore the dashed feedback path may be eliminated. This reduces the transfer function to

$$\frac{X}{V_{motor}} = \frac{K_T K_{BS} / n}{L_a J s^3 + (R_a J + D L_a) s^2 + (R_a D + K_T K_e) s}. \quad (3.2.2)$$

Therefore, Eq. (3.2.2) will be used as the system model to represent the actuator. This is a type one system, since it has an open loop pole at the origin. This ensures no steady state error for a unit step input when a position feedback loop is implemented in the closed loop. This indicates that in the steady state condition the actuator will act as a position servo.

3.3 Controller & Amplifier Model

A number of controllers and amplifiers were considered for use in this project. One option was constructing a linear amplifier and controller; another was purchasing either a pulse width modulated or linear amplifier with controller. A commercial pulse width modulated controller was selected because of availability and reasonable cost. The controller has five components: the power input, the lag-lead compensator, the pulse width modulated amplifier, jumper-selected torque or velocity control, and jumper-

selected tachometer (or other external input) or electronic EMF sensing. The functional block diagram appears in Fig. 3.3.1. The components are explained in the following segments.

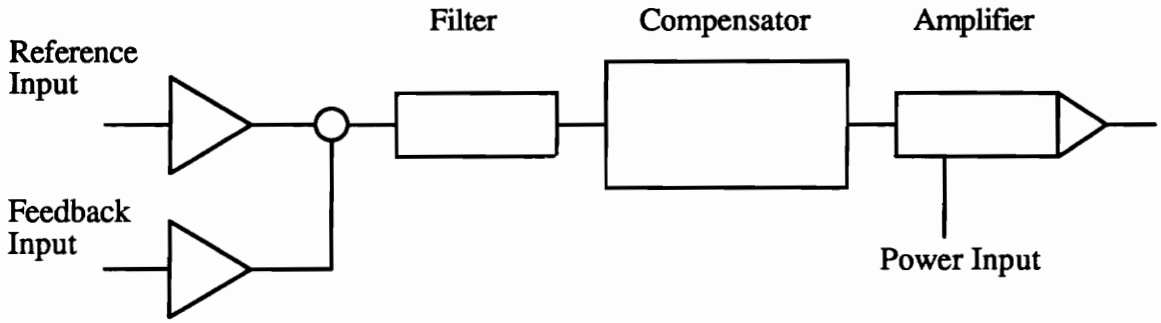

Figure 3.3.1: Controller Functional Block Diagram

The power input portion accepts either a low voltage, high current AC signal or a high current, low voltage DC supply. A 120V AC transformer provides power for up to three controllers. The amplifier also has a fault protection circuit which restricts output current and voltage to protect against short circuits.

The filter is shown in Fig. 3.3.2. The internal filter is a 100 Hz low pass filter, therefore, $1/T = 628$ rad/sec. This is acceptable for our system since the primary goal is static shape control. The filter circuit gain is -15.

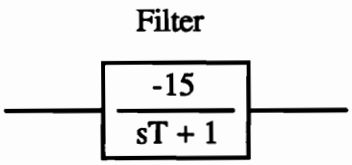

Figure 3.3.2: Filter Block Diagram

The compensator has adjustable lead and lag characteristics enabling a compromise between bandwidth, time response, and steady-state accuracy by using analog

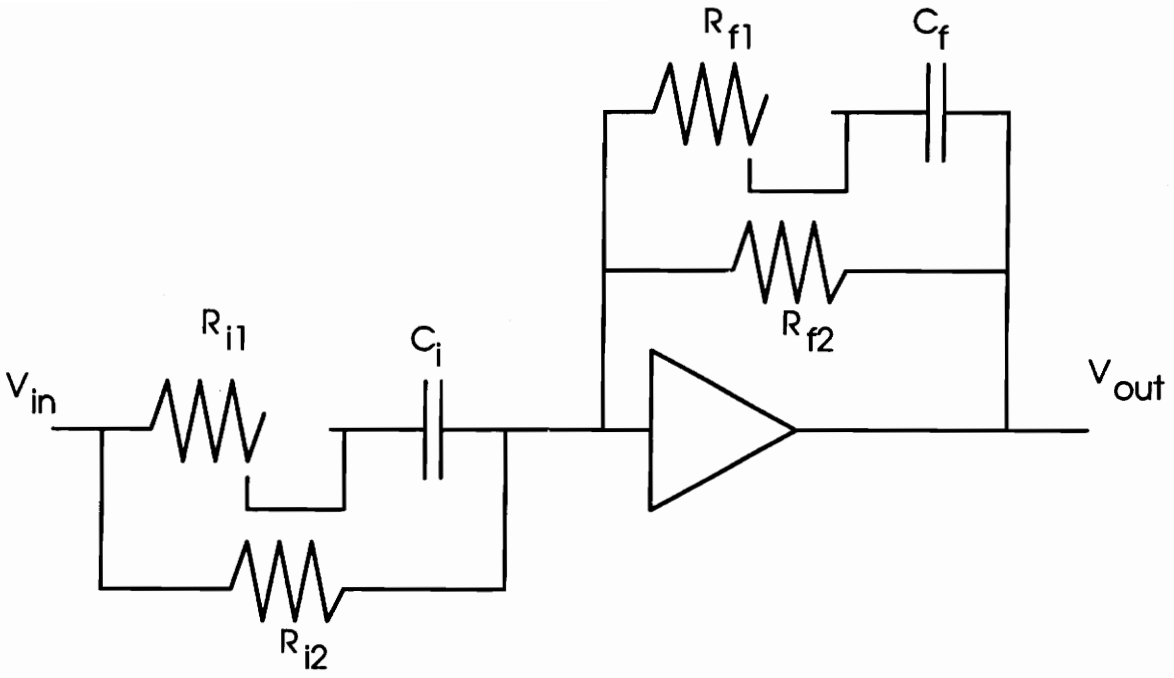

(a)

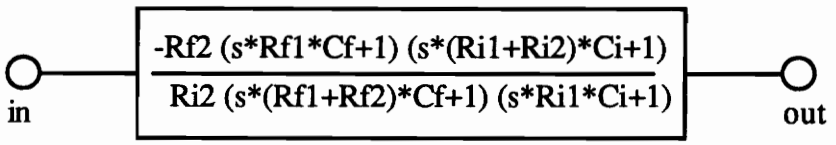

(b)

Figure 3.3.3: (a) Compensation Circuit in PMI Motor Amplifier
(b) Block Diagram of Compensator

potentiometers. The compensator circuit diagram is shown in Fig. 3.3.3. The resistive values, R_{i2} and R_{f2}, and the capacitive values, C_i and C_f, are fixed. Two potentiometers, R_{f1} and R_{i1}, allow adjustment of the lag-lead characteristics. From the diagram the compensator's transfer function is determined to be,

$$\frac{V_{Out}}{V_{In}} = \frac{R_{f2}\{[R_{f1}C_f(R_{i1}+R_{i2})C_i]s^2+[R_{f1}C_f+(R_{i1}+R_{i2})C_i]s+1\}}{R_{i2}\{[(R_{f2}+R_{f1})C_fR_{i1}C_i]s^2+[(R_{f2}+R_{f1})C_f+R_{i1}C_i]s+1\}} \qquad (3.3.1)$$

The compensator output is passed to the amplifier input. The pulse width modulated voltage amplifier is modeled as a simplified linear amplifier. With this model, it has an inverting gain of 100 and a current feedback of 0.5 volts/amp, as depicted in Fig. 3.3.4.

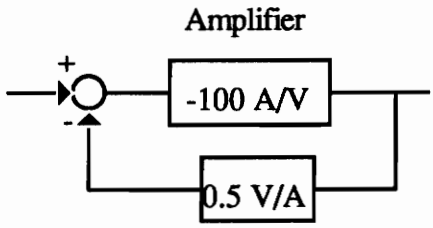

Figure 3.3.4: Amplifier Diagram

The back electromotive force (EMF) is inferred by using an electronic current sensing circuit. This circuit estimates the motor current and uses this for feedback in addition to the motor voltage information. This current is proportional to the back EMF produced in the motor, which is directly related to the motor velocity. Therefore this is an estimator for velocity feedback. This circuit has an adjustable potentiometer to calibrate it with motors of various characteristics by altering the feedback attenuation.

The additional feedback input is typically used when a tachometer is available for measured velocity feedback. In this experiment the controller is converted from a velocity servo to a position servo system. This is accomplished by replacing the tachometer feedback with a length sensor output and enabling both the EMF sensing

circuit for velocity feedback and the external input for position feedback. Alternatively, to allow a larger position feedback gain, the difference of the reference command and the position feedback may be input to the controller.

A single actuator block diagram of the overall system is shown in Fig. 3.3.5. Note that the actuators have been modeled without torque feedback into the drive shaft and therefore will act as a strict position servo regardless of the magnitude of spring constraints. This arrangement allows each actuator and controller to operate as a length-controllable member. Therefore, the steady state actuator extension responds linearly to the command signal.

3.4 Lumped Parameter Truss System Representation

The truss system is represented by a lumped parameter model. The actuator attachment points are retained in the model, and the elastic beam is modeled by discrete springs. One unmodeled quantity is the axial force applied from the actuators on the beams. This axial force is only significant if it is large and compressive since it could cause buckling. For the one actuator case at the far location, the minimum buckling load is 17,670 N. This is well above the loading available from the displacement ranges of the actuators. The truss with only one actuator will be modeled first, followed by the multi-actuator models.

Figure 3.4.1 depicts the physical system and the lumped parameter form for the case of the system with one actuator. A spring, with appropriate stiffness, replaces each beam section. The actuator attachment points are retained in the model. The extension of the lumped parameter model actuators represents the extension of the actual actuator perpendicular to the original orientation. By examining the equations for cantilevered

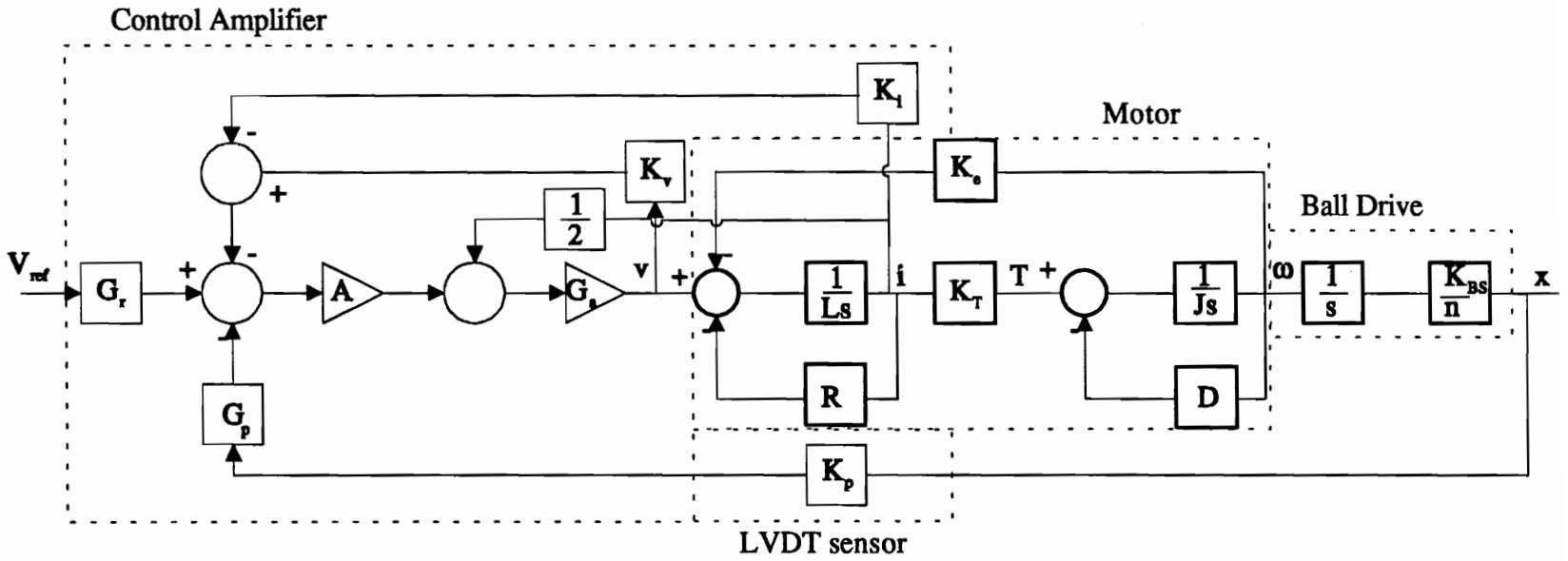

Figure 3.3.5: Closed-loop Actuator & Controller Block Diagram

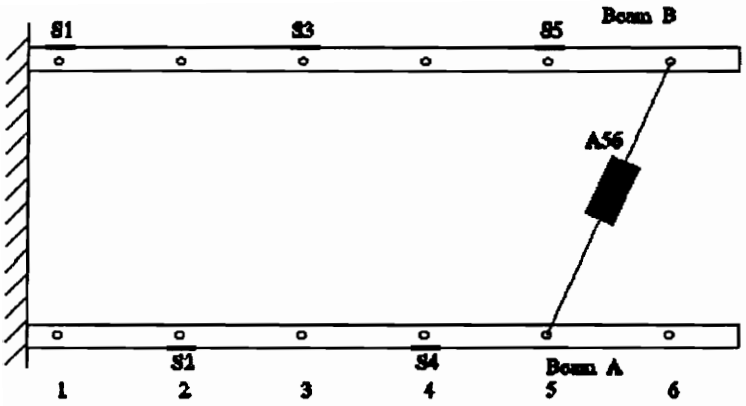

(a)

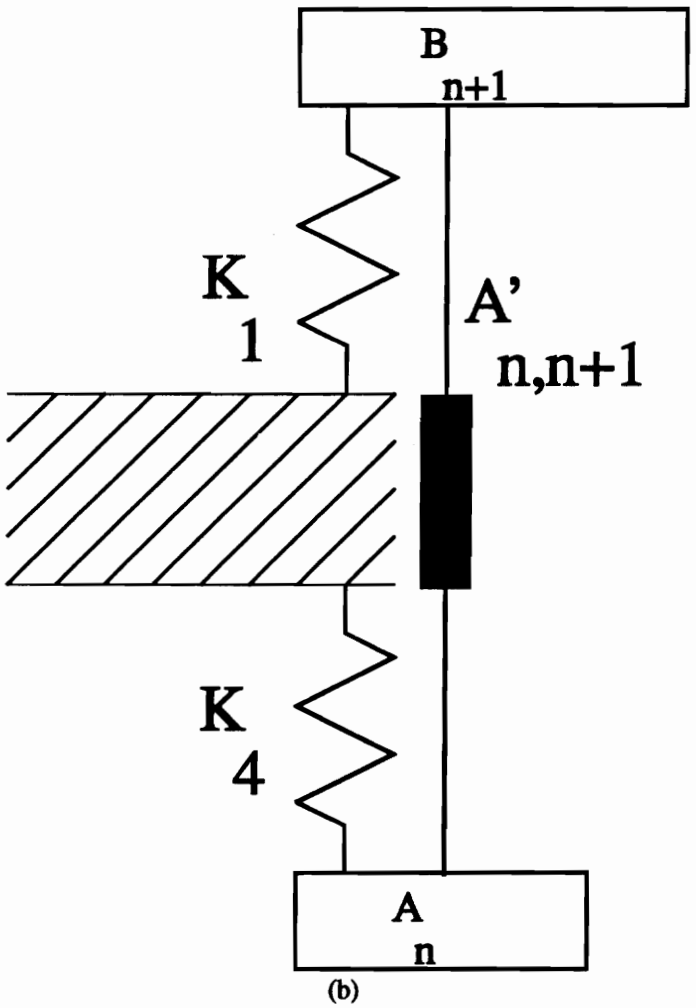

(b)

Figure 3.4.1 One Actuator Model
a. Beam Model
b. Lumped Parameter Model

beam deflection ($F = 3EI/L^3 * x$) and equating the lumped parameter model one can find the appropriate spring coefficients

$$k_1 = \frac{3EI}{L_{n+1}^3} \tag{3.4.1a}$$

$$k_4 = \frac{3EI}{L_n^3} \tag{3.4.1b}$$

Thereby a simplified lumped parameter model as Figure 3.4.1b can be examined for the one actuator case.

For an example, the equivalent constants are evaluated with one actuator located between A_5 and B_6. The material elasticity for aluminum is 71.0 GPa. The cross section has an area moment of inertia of 3603 mm^4. Point A_1 is 25.4 mm from the first support bolt, with each point is 102 mm from the closest point. This makes L_n = 432 mm and L_{n+1} = 533 mm. Thereby k_1 = 4.91 N/mm and k_4 = 9.26 N/mm. Since the extension of one actuator produces movements of both points the significant physical quantity is the ratio of the spring constants, k_4/k_1, which is 1.885.

A model of the beams connected by three actuators is developed next. The beam is depicted in Fig 3.4.2. The axial force components are neglected in the following equations. From strength of materials, the beam displacement equation for the lower beam is found to be,

$$\begin{aligned} EIY^A(x) = &+\frac{F_n^{AT}}{6}<x-L_n>^3 + \frac{F_{n+2}^{AT}}{6}<x-L_{n+2}>^3 \\ &-\frac{F_n^{AT}+F_{n+2}^{AT}}{6}x^3 + \frac{(F_n^{AT}L_n + F_{n+2}^{AT}L_{n+2})}{2}x^2 \end{aligned} \tag{3.4.2}$$

The other beam displacement equation is of the same form,

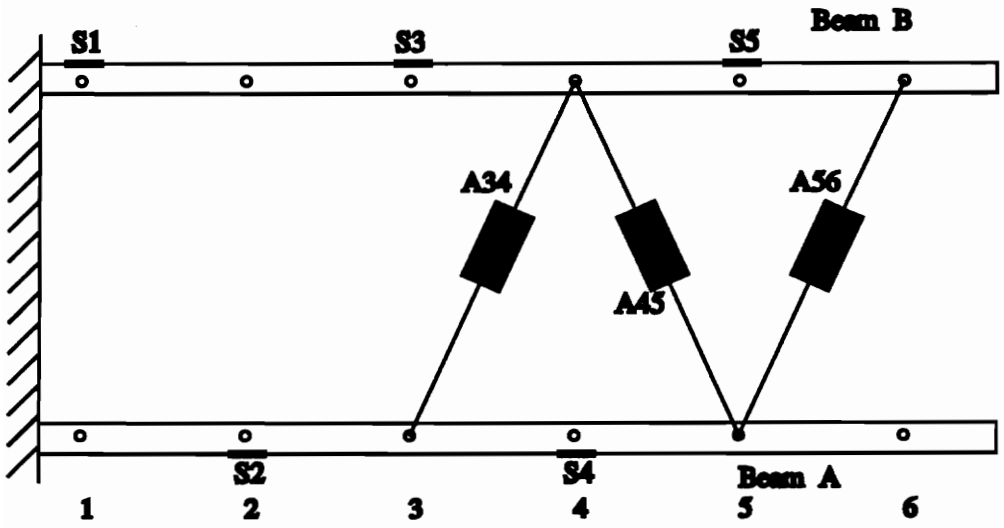

Figure 3.4.2: Beam experiment with three actuators

$$EIY^B(x) = +\frac{F^{BT}_{n+1}}{6}<x-L_{n+1}>^3 + \frac{F^{BT}_{n+3}}{6}<x-L_{n+3}>^3 - \frac{F^{BT}_{n+1}+F^{BT}_{n+3}}{6}x^3 + \frac{(F^{BT}_{n+1}L_{n+1}+F^{BT}_{n+3}L_{n+3})}{2}x^2 \tag{3.4.3}$$

Then solving these equations at the actuator attachment locations yields the following generalized matrix equation

$$\begin{bmatrix} Y^A_n \\ Y^A_{n+2} \\ Y^B_{n+1} \\ Y^B_{n+3} \end{bmatrix} = \begin{bmatrix} B_{11} & B_{12} & 0 & 0 \\ B_{12} & B_{22} & 0 & 0 \\ 0 & 0 & B_{33} & B_{34} \\ 0 & 0 & B_{34} & B_{44} \end{bmatrix} \begin{bmatrix} F^{AT}_n \\ F^{AT}_{n+2} \\ F^{BT}_{n+1} \\ F^{BT}_{n+3} \end{bmatrix} = \mathbf{BF} \tag{3.4.4}$$

The resulting flexibility matrix, in terms of the beam parameters, is

$$\mathbf{B} = \begin{bmatrix} \frac{L_n^3}{3EI} & \frac{-L_n^3+3L_n^2L_{n+2}}{6EI} & 0 & 0 \\ \frac{-L_n^3+3L_n^2L_{n+2}}{6EI} & \frac{L_{n+2}^3}{3EI} & 0 & 0 \\ 0 & 0 & \frac{L_{n+1}^3}{3EI} & \frac{-L_{n+1}^3+3L_{n+1}^2L_{n+3}}{6EI} \\ 0 & 0 & \frac{-L_{n+1}^3+3L_{n+1}^2L_{n+3}}{6EI} & \frac{L_{n+3}^3}{3EI} \end{bmatrix} \tag{3.4.5}$$

This matrix relates the nodal forces to the nodal displacement. The simplified system is shown in Fig. 3.4.3. From a free body diagram, the equation of motion of this spring system is

$$\begin{bmatrix} F^{AT}_n \\ F^{AT}_{n+2} \\ F^{BT}_{n+1} \\ F^{BT}_{n+3} \end{bmatrix} = \begin{bmatrix} k_4+k_5 & -k_5 & 0 & 0 \\ -k_5 & k_5+k_6 & 0 & 0 \\ 0 & 0 & k_1+k_2 & -k_2 \\ 0 & 0 & -k_2 & k_2+k_3 \end{bmatrix} \begin{bmatrix} Y^A_n \\ Y^A_{n+2} \\ Y^B_{n+1} \\ Y^B_{n+3} \end{bmatrix} = KY \tag{3.4.6}$$

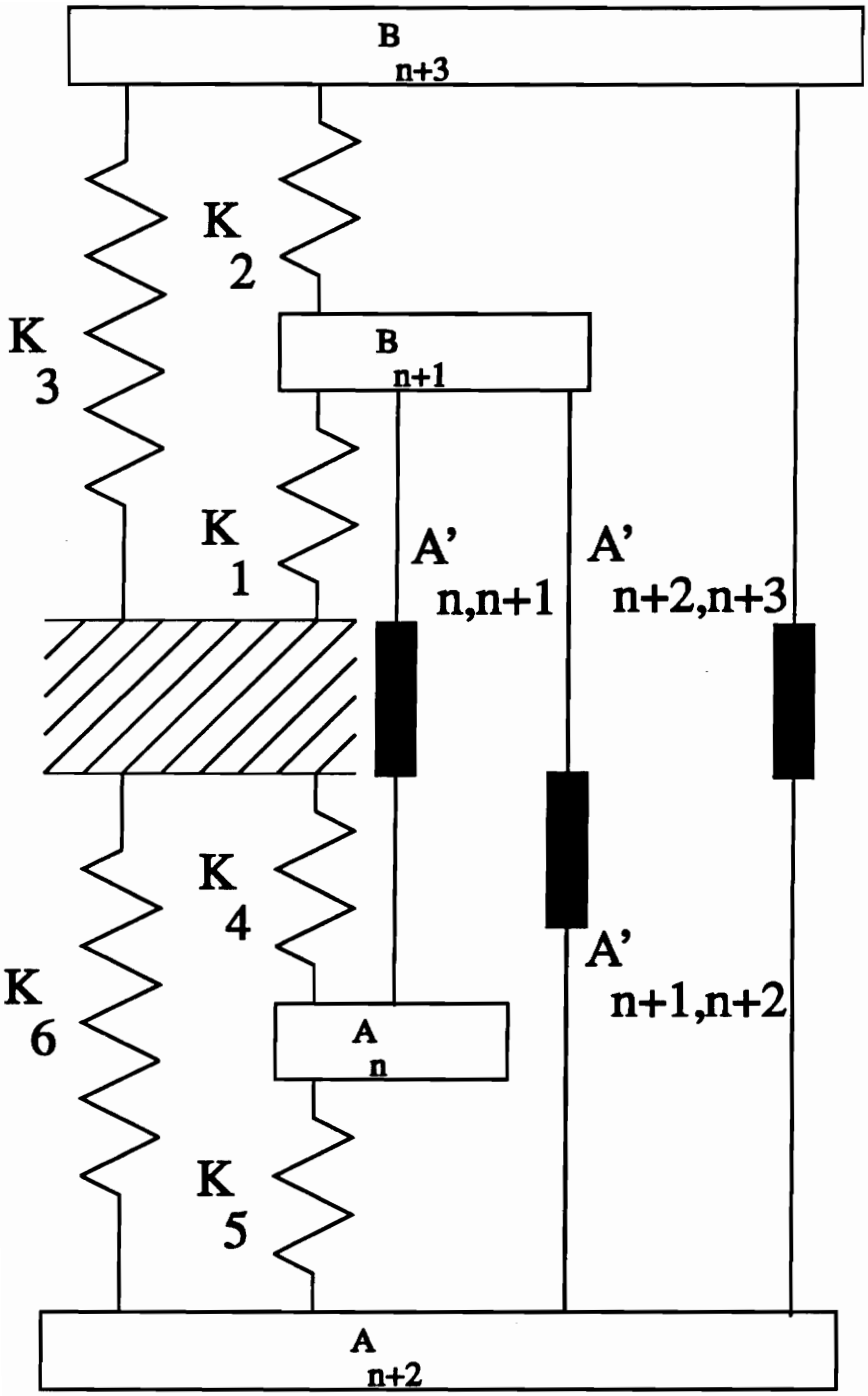

Figure 3.4.3: Lumped Parameter Spring-Actuator System

By equating the inverted stiffness matrix ($\mathbf{K^{-1}}$) and the flexibility matrix (**B**) the spring coefficients are found to be,

$$k_1 = \frac{B_{44} - B_{34}}{B_{33}B_{44} - B_{34}^2} \tag{3.4.7a}$$

$$k_2 = \frac{B_{34}}{B_{33}B_{44} - B_{34}^2} \tag{3.4.7b}$$

$$k_3 = \frac{B_{34} - B_{33}}{B_{33}B_{44} - B_{34}^2} \tag{3.4.7c}$$

$$k_4 = \frac{B_{22} - B_{12}}{B_{11}B_{22} - B_{12}^2} \tag{3.4.7d}$$

$$k_5 = \frac{B_{12}}{B_{11}B_{22} - B_{12}^2} \tag{3.4.7e}$$

$$k_6 = \frac{B_{12} - B_{11}}{B_{11}B_{22} - B_{12}^2} \tag{3.4.7f}$$

The flexibility terms may be replaced with the physical parameters to yield numerical results. The spring constants are calculated for a system with three actuators between points A_3 and B_4, points B_4 and A_5, and points A_5 and B_6. In this case, n, the first attachment point, is 3. These values may be calculated since the **B** matrix is solely composed of structural parameters. The length parameters are $L_n = 228$ mm, $L_{n+1} = 330.2$ mm, $L_{n+2} = 431.8$ mm, $L_{n+3} = 533.4$ mm. These values are

$k_1 = 91.7$ N/mm
$k_2 = 77.1$ N/mm
$k_3 = -36.9$ N/mm
$k_4 = 212.$ N/mm
$k_5 = 112$ N/mm
$k_6 = -64.3$ N/mm

As shown in the diagram, k_3 and k_6 represent the additional stiffness to ground of the more distant beam points. The negative spring constant, although unrealizable as a single

component, represents the fact that points further from the root of the beam have decreased stiffness to ground. A negative value simply reduces the effective stiffness of the distant point in relation to the closer point. Figure 3.4.4 shows one mass with two springs to ground. In this example k_2 may be negative as long as k_1 has a larger positive amplitude. This is simply a modeling convenience which is valid in the mathematical model.

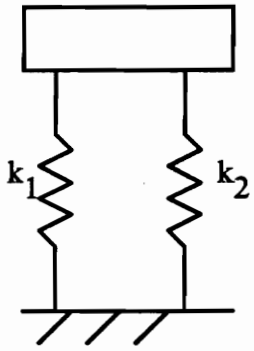

Figure 3.4.4: Double spring system example

For a two actuator case as depicted in Fig. 3.4.5, the spring constants for the structure are found as $k_1 = 91.7$ N/mm, $k_2 = 77.1$ N/mm, $k_3 = -36.9$ N/mm, $k_4 = 9.26$ N/mm. The lumped parameter model is presented in a general form with n indicating the first actuator attachment point. In this example, with the two furthest actuators being used, n is 4.

3.5 Displacements from Strain Measurements

The relationship between the strain gage output and the beam displacements is derived in this section. This relation is necessary to replace the length (LVDT) feedback with the strain signals. The displacement and force relationship was previously shown as

$$\mathbf{Y} = \mathbf{BF}. \tag{3.5.1}$$

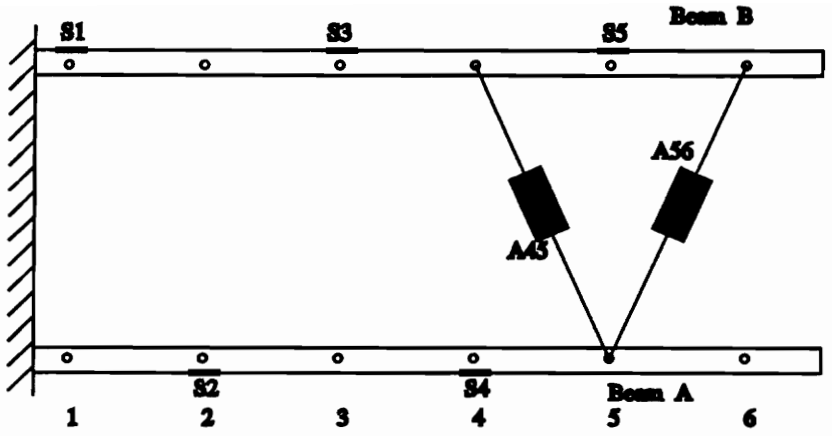

(a)

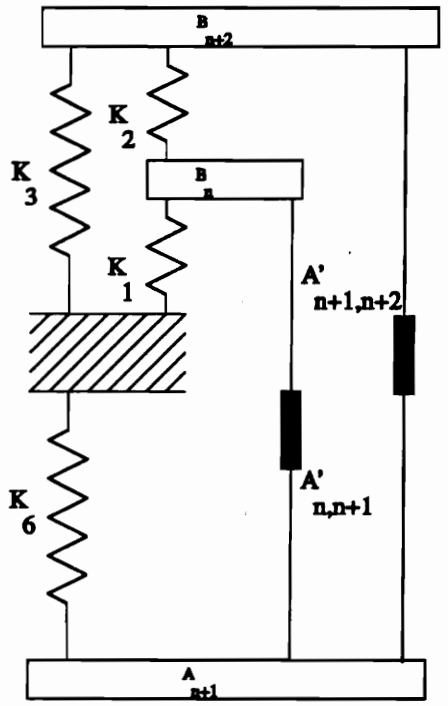

(b)

Figure 3.4.5: Two Actuator Model
a. Beam Model
b. Lumped Parameter Model

The strain gages are located across from the attachment points on the opposite beam. They were placed there to be equidistant from the actuator attachment points. One attachment is at point A_5 so a strain gage is placed at location B_5. The strain gages are positioned as drawn in Fig 3.4.2 and labeled S_n. The relation between the moment at the strain gage sensors and the transverse forces from the actuators is found from the basic moment equations to be,

$$\begin{bmatrix} M^A_{n-1} \\ M^A_{n+1} \\ M^B_n \\ M^B_{n+2} \end{bmatrix} = \begin{bmatrix} L_n - L_{n-1} & L_{n+2} - L_{n-1} & 0 & 0 \\ 0 & L_{n+2} - L_{n+1} & 0 & 0 \\ 0 & 0 & L_{n+1} - L_n & L_{n+3} - L_n \\ 0 & 0 & 0 & L_{n+3} - L_{n+2} \end{bmatrix} \begin{bmatrix} F^{AT}_n \\ F^{AT}_{n+2} \\ F^{BT}_{n+1} \\ F^{BT}_{n+3} \end{bmatrix} = LF \quad (3.5.2)$$

The strain gages were configured to measure bending strain, so the output is proportional to the bending moment at the measured points. The strain voltage is directly related to the point moments, as found from the flexural formula. The electronic gains, from the strain conditioner, and structural parameters can be combined in diagonal matrix, as

$$V_{\varepsilon_{bending}} = \begin{bmatrix} \frac{1}{g_1} & 0 & 0 & 0 \\ 0 & \frac{1}{g_2} & 0 & 0 \\ 0 & 0 & \frac{1}{g_3} & 0 \\ 0 & 0 & 0 & \frac{1}{g_4} \end{bmatrix} \begin{bmatrix} \frac{EI_{zz\ local}}{y} & 0 & 0 & 0 \\ 0 & \frac{EI_{zz\ local}}{y} & 0 & 0 \\ 0 & 0 & \frac{EI_{zz\ local}}{y} & 0 \\ 0 & 0 & 0 & \frac{EI_{zz\ local}}{y} \end{bmatrix} \begin{bmatrix} M^A_{n-1} \\ M^A_{n+1} \\ M^B_n \\ M^B_{n+2} \end{bmatrix} = G^{-1}M \quad (3.5.3)$$

The $I_{zz\ local}$ is the area moment of inertia at the strain gage. In this experiment the gages were mounted above a drilled hole and had a lower I_{zz} than the solid portion of the beam. The area moment at the center of the hole is 2854 mm^4. From the above

equations the displacement at the actuator points given the measured bending strain voltage is

$$Y = BL^{-1}GV_{\varepsilon_{bending}} \tag{3.5.4}$$

From the kinematic equations the actuator extensions can be evaluated.

$$\delta = E_3 Y = E_3 (BL^{-1}G)V_\varepsilon \tag{3.5.5}$$

where E_3 is the linear transformation from the point displacements to the actuator extensions. This is a rectangular matrix since there are n strain readings for n-1 actuators. This matrix equation may then be evaluated to provide length control of each position servo based on multiple strain gage outputs. In our case, for three actuators the equation becomes,

$$\begin{bmatrix} \delta_{34} \\ \delta_{45} \\ \delta_{56} \end{bmatrix} = J \begin{bmatrix} 5.20 & -5.60 & 1.73 & -1.15 \\ 5.20 & -5.60 & 4.03 & -0.45 \\ 10.0 & -8.08 & 4.03 & -0.45 \end{bmatrix} \begin{bmatrix} V_{\varepsilon B3} \\ V_{\varepsilon B5} \\ V_{\varepsilon A2} \\ V_{\varepsilon A4} \end{bmatrix}, \tag{3.5.6}$$

where J is a scaling variable based on the structural parameters and the desired electronic gain. J will not effect the steady state response. For two actuators the gain matrix becomes

$$\begin{bmatrix} \delta_{45} \\ \delta_{56} \end{bmatrix} = J \begin{bmatrix} -4.47 & 4.82 & 10.0 \\ -8.60 & 6.95 & 10.0 \end{bmatrix} \begin{bmatrix} V_{\varepsilon B3} \\ V_{\varepsilon B5} \\ V_{\varepsilon A4} \end{bmatrix} \tag{3.5.7}$$

These relations may then be used to calculate actuator extension based on a set of strain readings instead of the LVDT signal.

3.6 Modeling Summary

The system components were modeled using transfer functions and a lumped parameter model. The system block diagram was shown for one actuator. The dynamic

components are modeled such that the strain feedback may replace the LVDT feedback. The lumped parameter model for one, two, and three actuators will be contrasted to the experimental results. The relations for replacing LVDT feedback with strain feedback were derived.

Chapter 4
Experimental Results & Discussion

4.1 Experimental Overview

This chapter explains the experiments and discusses the results. The first goal is to confirm the actuator-beam displacement model. The second goal is to replace the actuator length (LVDT) signal with the beam strain gage readings for control. The experiments are described below.

The first experiment is to find the relation between a reference command signal input to the actuator and the resulting length of the actuator-sensor pair. The repeat confidence levels of the length of an unattached actuator are found in response to the applied voltage. The second experiment uses a micrometer to evaluate the confidence bounds of the beam displacement measurements. The third experiment uses one actuator and length feedback to confirm the beam displacement model.

The next group of experiments examine the multi-actuator beam displacement model. A two actuator model is compared to an experiment, and then a three actuator model is compared to an experiment. The experiment compares actuator extensions to the resulting measured deformations. The two and three actuator cases are examined using position feedback.

In the final experiments, strain gages mounted on the beams are used to provide feedback. The resulting beam displacements are compared to the experiments where the LVDT was used for the position feedback to demonstrate that the LVDT sensors may be replaced by the strain gages.

4.2 Measurement Calibration

4.2.1 Actuator and Sensor Calibration

This experiment is done to determine if the actuator calibration is linear and to find the coefficients. This is necessary in further experiments for predicting the actuator extensions. The configuration was found to be insensitive to the loading conditions found in this experiment.

The actuator extension reproducibility is examined with the actuators unattached. There are two cases which will be examined, a low gain and a high gain configuration. A set of command voltages are repeated, first ascending and then descending. A micrometer is used to measure the distance between the clevis ends for these command signals. In this first case, the actuator length (LVDT) signal is used in the feedback path as depicted in Fig. 4.2.1, which sends the signal to an internal controller summer. The LVDT signal, command voltage, and measured extension are recorded. The confidence bounds of the length measurements are evaluated. Next, the linear regression parameters are evaluated between the command signal and the measured extension, as well as the sensor signal and the measured extension.

Table 4.2.1 displays the mean actuator extension, standard deviation, and 95% confidence bounds for each input voltage. These confidence bounds relate the command voltage and resulting extension. The largest confidence bounds are ± 0.27 mm for repeating a specific extension. This range may be reduced by increasing the feedback gain on the sensor output. This will be addressed in a second configuration following the low gain case.

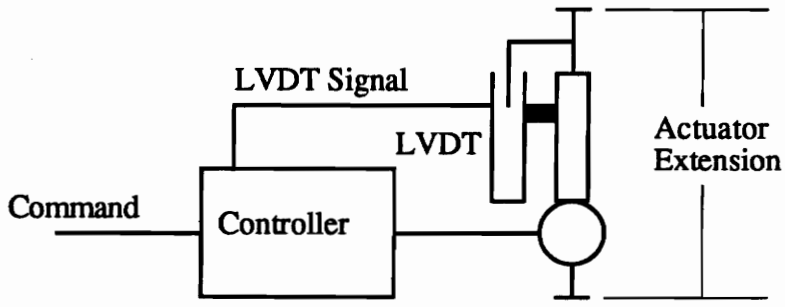

Figure 4.2.1: System Circuit with Internal Jumper

Table 4.2.1: 95% Confidence Bounds of LVDT Control Using Repeat Command Signals

Command Signal (Volts)	Mean Length for Group (mm)	Standard Deviation (mm)	95% Confidence Bounds	
			Low (mm)	High (mm)
-2.010	249.24	0.07	249.16	249.31
-1.005	255.61	0.19	255.41	255.81
0.001	262.09	0.19	261.89	262.28
1.005	268.59	0.26	268.32	268.86
2.010	274.91	0.17	274.71	275.11

Table 4.2.2: Command Sensitivity with Low Gain

		95% Confidence Bounds
Actuator Calibration	6.40	±0.05 mm/v
Actuator Offset	262.09	±0.07 mm
Correlation Coefficient	0.9996	

The linear regression parameters for the command signal and the measured length relation are shown in Table 4.2.2. The actuator calibration is 6.40 ± 0.05 mm/v. Less than a 0.8% variation in the slope covers the 95% confidence bounds.

Next the LVDT sensor is calibrated. The parameters for the sensor voltage and measured length linear relation are shown in Table 4.2.3. The correlation coefficient for the sensor fit is 1.0000. The variation in the calibration for the sensor is less than 0.2% across the 95% confidence bounds. This indicates that for the actuator-LVDT-controller configuration with the internal jumper, the LVDT sensor signal-to-extension relation is more precise then the reference command-to-extension relation. These tables reveal that the sensor parameters from the linear fit are 3.16 ± 0.004 mm/V with an offset of 262.09 ± 0.01 mm. The parameters for the command signal-to-extension relation are 6.40 ± 0.05 mm/V and 262.09 ± 0.07 mm. The sensing confidence bounds are less than one sixth that of the control confidence bounds.

Table 4.2.3: LVDT Sensitivity with Low Gain

		95% Confidence Bounds
Actuator Calibration	3.16	±0.004 mm/V
Actuator Offset	262.09	±0.012 mm
Correlation Coefficient	1.0000	

Table 4.2.4.: 95% Command Confidence of LVDT Control with External Summation

Command Voltages	Mean Length for Group (mm)	Standard Deviation (mm)	95% Confidence Bounds	
			Low (mm)	High (mm)
-2.999	274.87	0.04	274.83	274.92
-1.999	270.62	0.02	270.60	270.65
-0.998	266.37	0.07	266.31	266.44
0.002	262.19	0.03	262.16	262.21
1.000	257.98	0.04	257.93	258.02
2.000	253.69	0.04	253.65	253.73
3.000	249.43	0.09	249.34	249.53

To provide smaller confidence bounds for the linear regression parameters from the command signal-to-extension relation, the gain on the LVDT signal was increased. By experimental observation the feedback signal clips in the amplifier with increased gain. Therefore, an external summing circuit is used. A block diagram is shown in Figure 4.2.2. The difference between the amplified feedback signal and the command voltage is then sent to the controller input. The processed data appears in Table 4.2.4. Seven repeat points are used in this calibration. The range of the command signals were increased, due to the higher gain, to calibrate the same extensions as the first case. Compared with the first arrangement it shows a decrease in the standard deviation and the confidence boundaries for individual points. The maximum confidence bounds were ±0.27 mm with the internal summer and ±0.10 mm using the external summer. The gain was increased from 0.5 to 1.

Table 4.2.5 tabulates the linear fit coefficients for the command voltage calibration. The parameters of this fit have a smaller range for the coefficient confidence limits than with the internal jumper. The slope changed significantly from Table 4.2.2 since the gain was increased and there was a signal inversion. Table 4.2.6 lists the regression parameters between the sensor signal and the output length. These confidence bounds on the regression parameters are on the same order as that of the high gain command calibration.

Table 4.2.5: Command Calibration with High Gain

		95% Confidence Bounds
Actuator Calibration	-4.24	±0.02 mm/v
Actuator Offset	262.17	±0.04 mm
Correlation Coefficient	1.000	

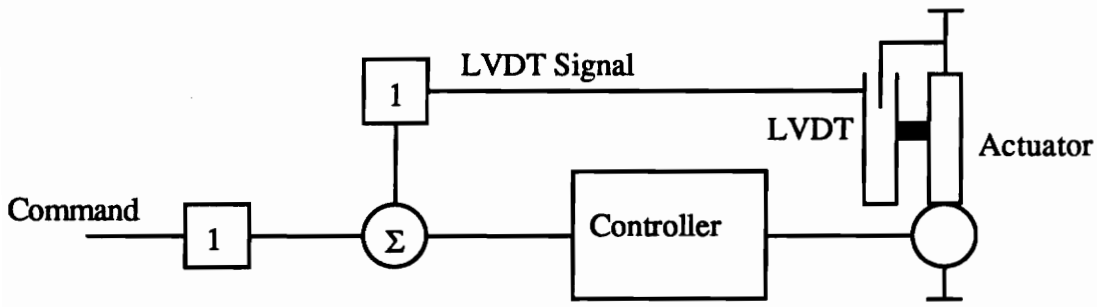

Figure 4.2.2: High Gain Controller Configuration

Table 4.2.6: LVDT Sensor Calibration with High Gain

		95% Confidence Bounds
Actuator Calibration	4.24	±0.02 mm/v
Actuator Offset	262.17	±0.03 mm
Correlation Coefficient	1.000	

Throughout the experiments the primary measurement is the LVDT sensor signal. The coefficient confidence bounds relating the LVDT voltage and the extension are below 0.5% variation of the slope in each of the above tests. Also, in both cases the regression coefficient is 1.000. The sensor-to-extension relationship is comparable in both the low and high gain case, as expected. The experiments use the low gain configuration because it is a simple circuit and the primary measurement is the LVDT sensor from which the actuator length is computed and this is unaffected by the gain selection. Henceforth, there is no loss of precision based on the implementation.

4.2.2 Beam Displacement Measurement Accuracy

The measurement of the beam displacements is a critical aspect of the experiment. In order to demonstrate the repeatability of measuring from the reference wire to the beam two samples are taken prior to having any actuator installed.

Table 4.2.7 lists the mean distance and standard deviations from the reference wire to the beam at points A_5 and B_6. Ten measurements were made for each location. For the two distances chosen, the 95% confidence bounds are less than ±0.03 mm.

Table 4.2.7: Mean and Standard Deviations of Beam Displacement Measurements

	Displacement of A_5 (mm)	Displacement of B_6 (mm)
Mean	26.80	25.15
Standard Deviation	0.05	0.04
±95% Confidence Bounds	0.03	0.03

4.3 LVDT Length Feedback

LVDT feedback is the most direct method to control the length of the actuator extensions for various loads. The output of the LVDT sensor may be directly input to the feedback path of the commercial controller. This was done as part of the prior calibration using the controller's internal summer. The purpose of these experiments is to confirm the system displacement model. The experiments with one, two, and three actuators follow.

4.3.1 Single Actuator with LVDT Feedback

The first model to be confirmed is the single actuator case. This is shown in Fig. 4.3.1a. In order to limit the beam strain levels the actuator is placed in position A_{56}. The lumped parameter model, depicted in Fig. 4.3.1b, has two springs, two points and an actuator. The theoretical equivalent spring values, found from the beam parameters, are k_1 = 4.910 N/mm and k_4 = 9.257 N/mm. The ratio of these spring constants is significant in contrasting the deflection of one point relative to the other. The calculated ratio, k_4/k_1, is 1.885.

The beam displacements are compared with a model. The model accounts for the geometry and attachment position of the actuator. A linear regression is then performed to find the beam displacement-to-actuator extension coefficients. The linear regression coefficients may be compared with the linear models presented. The average and

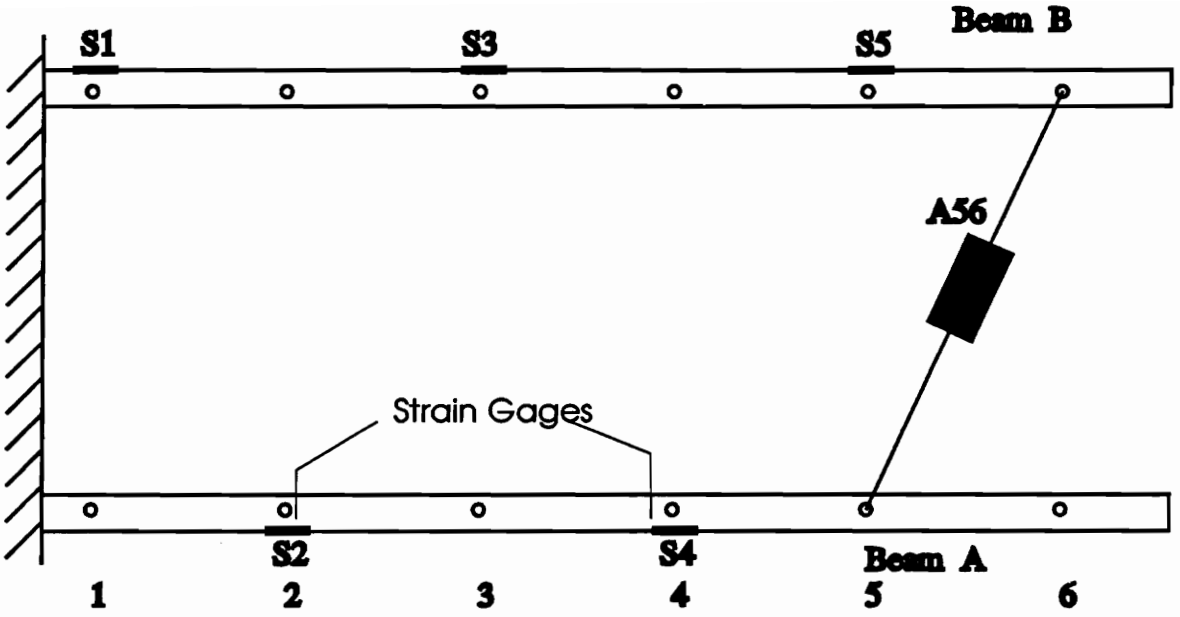

(a)

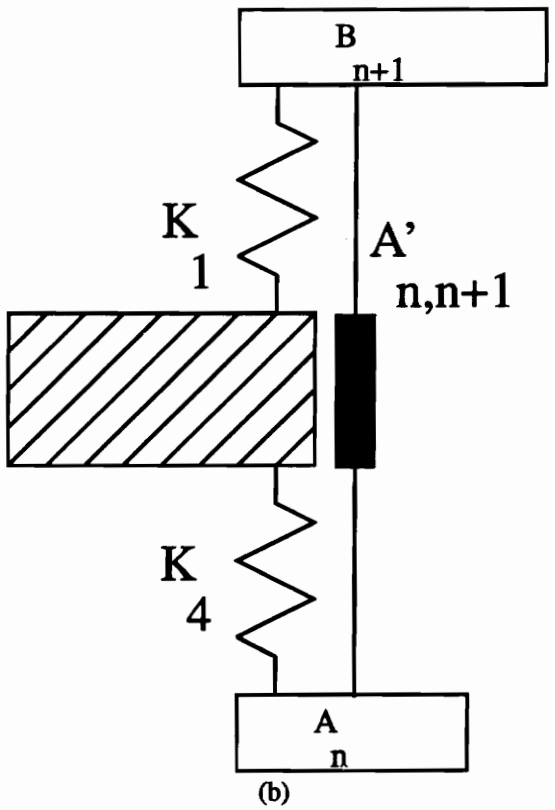

(b)

Figure 4.3.1 One Actuator Model
a. Beam Model
b. Lumped Parameter Model

standard deviation of the residuals are also reported. The experiment is done with the actuator in position A_{56} and then in position A_{45}. One test measures the actuator bolt-to-bolt length using the micrometer and compares this to the calibrated extension from the LVDT measurement. This is to determine whether there is any joint gap.

The experiments in section 4.2 showed that the sensor responds in a linear fashion, therefore a calibration may be performed prior to each experiment. The sensor is calibrated by recording a set of LVDT sensor signals and actuator lengths, prior to being mounted to the beams. The LVDT voltage-to-extension linear fit may be used to calculate the actuator extensions for various sensor signals. The beam strain gages are zeroed when the actuator is unattached. The actuator clevises are then attached with studs to the beams. Once attached, the actuator is adjusted to reduce the strain gage readings to zero at all the gages. This beam position and actuator length are then recorded and used as the unstrained condition. A zero strain level is not always recovered because of the cross sensitivity of the gages to the transverse strain caused by the weight of the actuator.

The actuator is then moved through its range of motion and the beam displacements, strain gage readings, and LVDT sensor readings are recorded. The beam displacements are measured at actuator attachment points A_5 and B_6. The extension and displacements are zero at the unstrained condition. The theory predicts that the displacement between the two actuator end points, Δy, will be greater than the actuator extension, $\Delta\delta$. This result is due to the kinematics of the structure. Figure 4.3.2 depicts the effect. The change of displacement, Δy, is

$$\Delta y = \sqrt{(\delta + \Delta\delta)^2 - x^2} - \sqrt{\delta^2 - x^2} \qquad \text{(Eq. 4.2.1)}$$

where y is the distance between the undeformed beams, Δy is the change of distance between the beams, δ is the undeformed actuator length, $\Delta\delta$ is the actuator extension, and x is the spacing between attachment locations. A number of these parameters are constants in these experiments the distance between the undeformed beams, y, the undeformed actuator length, δ, and the spacing between points, x. The spacing between points along the beam is constant since the beams are assumed stiff in the longitudinal direction.

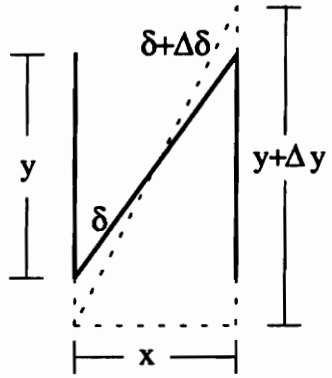

Figure 4.3.2: Actuator Kinematic Effect

The actuator angle results in the displacement of the attachment points, Δy, being larger than $\Delta\delta$. Table 4.3.1 presents the results of the single actuator model with the kinematic relation and the experimental average residual and standard deviation of the residual. Upon linearizing the kinematic relationship with the fixed parameters the constant of proportionality between the actuator extension and the displacements of locations A_5 and B_6 are -0.381 mm/mm and 0.719 mm/mm for, $\Delta\delta$, ±25.4 mm extension. The difference between the predicted movement and the actual displacement is the residual. The average and standard deviation of these residuals is a measure of how close the theory is predicting the response. The average residual for point A_5 is -0.08 mm with a residual standard deviation of 0.23 mm. Point B_6 has an average residual of 0.17 mm and a

residual standard deviation of 0.41 mm. The primary source of error is the joint gap, which will be examined in a further test.

Table 4.3.1: Point Displacement and A_{56} Actuator Extension -- Model

	A_5	B_6
Slope	-0.381 mm/mm	0.719 mm/mm
Intercept	0.00 mm	0.00 mm
Ratio of Slopes	1.885	
Average Residual	-0.08 mm	0.17 mm
Standard Deviation of Residual	0.23 mm	0.41 mm

Table 4.3.2 presents the coefficients of a fit between the point displacements and the actuator extensions. The coefficient for the displacement at A_5 and B_6 are -0.346 and 0.652, respectively. The confidence bounds for each of the calculated coefficients is also tabulated. The ratio of the slopes for the linear fit is 1.883 which indicates that the displacement ratios are as predicted. This indicates that the beam model is correct for the displacement of each point relative to the other.

Table 4.3.2: Point Displacement and A_{56} Actuator Extension -- Experiment

	A_5	B_6
Slope	-0.346 mm/mm	0.652 mm/mm
95% Confidence Bounds	0.011 mm/mm	0.017 mm/mm
Intercept	0.000 mm	0.000 mm
95% Confidence Bounds	0.06 mm	0.10 mm
Coefficient of Correlation	0.995	0.997
Ratio of Slopes	1.883	
Average Residual	-0.04 mm	0.07 mm
Standard Deviation of Residuals	0.12 mm	0.17 mm

In order to demonstrate that the system is responding in a linear fashion between the actuator extensions and the point displacements, Fig. 4.3.3 examines the displacements as a function of the actuator extension. This figure shows the individual data points and the

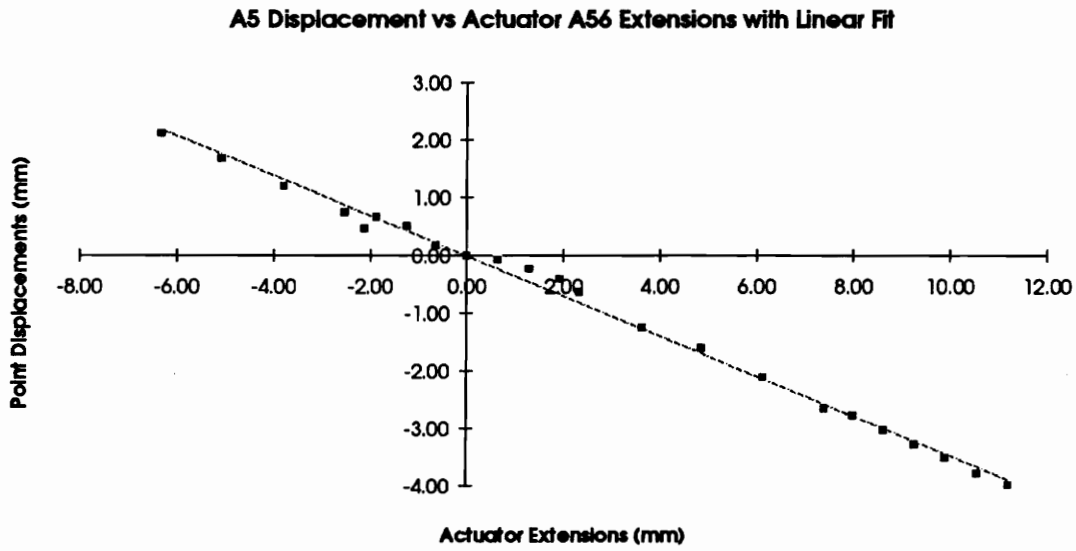

(a)

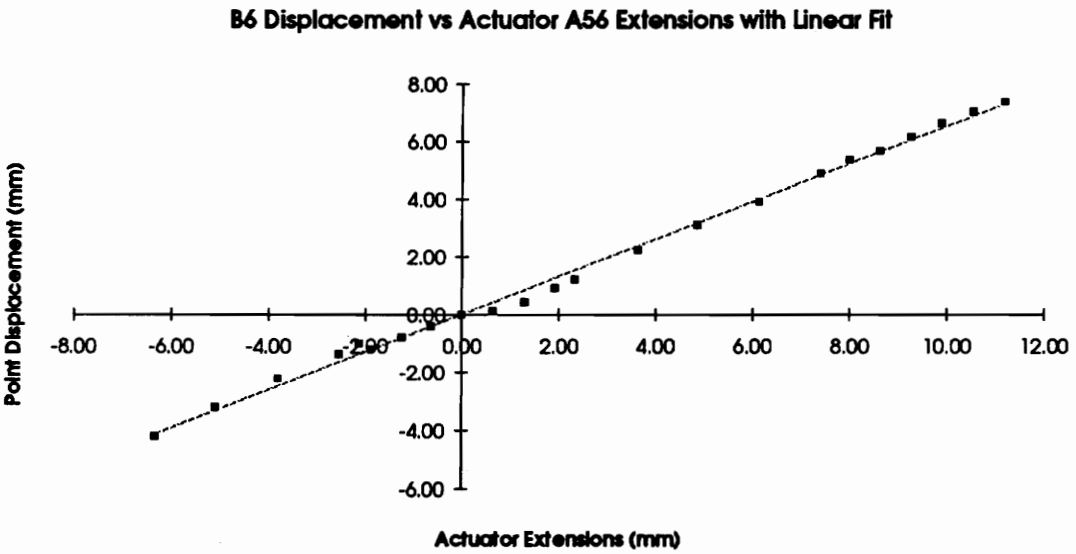

(b)

Figure 4.3.3: Point Displacement vs Actuator A_{56} Extensions
(a) Point A_5
(b) Point B_6

best fit line. The ratio of these slopes should equal the theoretical spring constant ratio. From the experiment, the ratio of the slopes is 1.883 compared to the modeled result of 1.885. This confirms the beam displacement model for the single actuator case.

This experiment is also run with the actuator in position A_{45}. Table 4.3.3 arranges the results from the model and the experimental residuals. In the model the constant of proportionality between the extension and A_5 and B_4 displacements are 0.760 mm/mm and -0.340 mm/mm. The average residual for A_5 is 0.01 mm and the standard deviation is 0.44 mm. The average residual for B_4 is -0.08 mm and the standard deviation is 0.22 mm.

Table 4.3.3: Point Displacements to A_{45} Actuator Extensions -- Model

	A_5	B_4
Slope	0.760 mm/mm	-0.340 mm/mm
Intercept	0.000 mm	0.000 mm
Ratio	2.236	
Average Residual	0.01 mm	-0.08 mm
Standard Deviation of Residuals	0.44 mm	0.22 mm

Table 4.3.4 presents the linear fit of the displacements to the calibrated extension. The slopes from the A_5 and B_4 fit are 0.653 mm/mm and -0.285 mm/mm. Figure 4.3.4 demonstrates the data points and the best linear fit for each set.

Table 4.3.4: Point Displacement to A_{45} Actuator Extensions -- Experimental

	A_5	B_4
Slope	0.653 mm/mm	-0.285 mm/mm
95% Confidence Bounds	0.034 mm/mm	0.015 mm/mm
Intercept	0.000 mm	-0.003 mm
95% Confidence Bounds	0.005 mm	0.002 mm
Ratio of Slopes	2.291	
Average Residual	0.00 mm	0.00 mm
Standard Deviation of Residuals	0.17 mm	0.08 mm

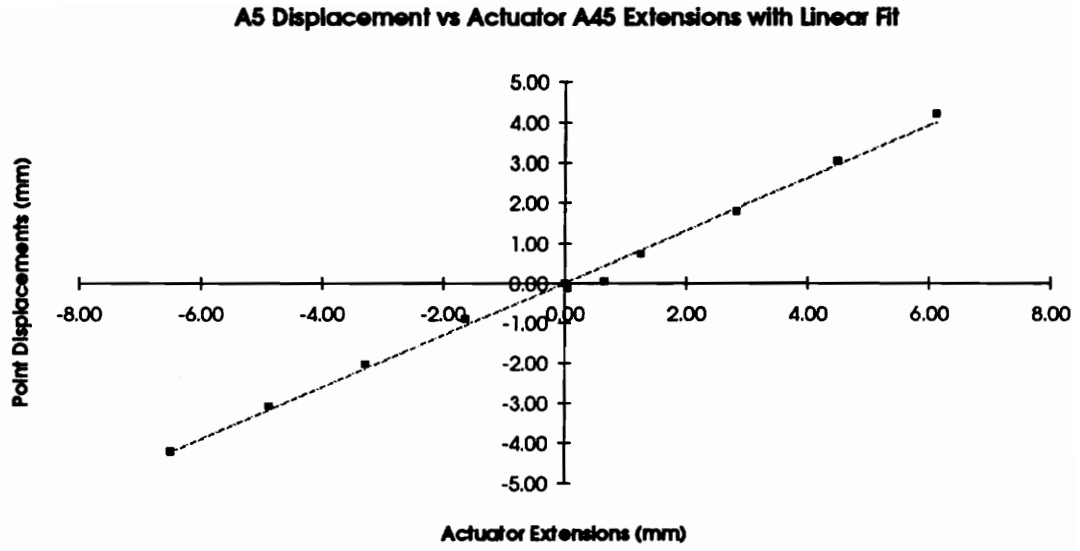

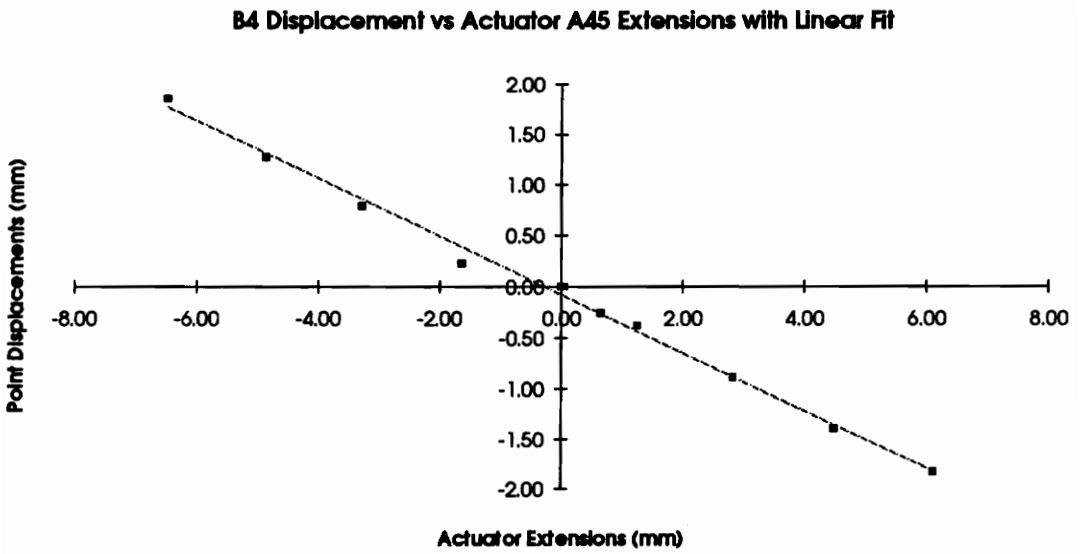

Figure 4.3.4: Point Displacements vs Actuator A_{45} Extensions
(a) Point A_5
(b) Point B_4

In a further experiment to check joint nonlinearity the actuator was calibrated prior to attachment by measuring the outside bolt-to-bolt distance. The first fifteen points are utilized for the linear interpolation. During actual operation the distance is measured between the bolts to check the linear model. The discrepancies between the actual measurements and the linear model are listed as an apparent gap and these results are presented in Table 4.3.5. There appears to be two distinct groupings of the data. This first part of the data has all positive apparent gaps while the second part has all negative values. This indicates that it is a gap that accounts for the nonlinearity. Therefore this illustrates a systematic error when using LVDT feedback.

4.3.2 Two Actuators with LVDT Feedback

This experiment checks the multi-actuator displacement model. The experiment uses actuators in both positions A_{45} and A_{56}. The actuators are placed in the positions which the lowest strains occur. This configuration enables independent specification of two point displacements. Unlike the first experiment in which the attachment point locations are linearly dependent on each other, now two displacements are independent. This means that the beams may take on different contours.

The lumped parameter model and system diagram are shown in Fig. 4.3.5. Based on the beam parameters, the equivalent spring constants for this configuration are $k_6 = 9.257$ N/mm, $k_1 = 91.76$ N/mm, $k_2 = 76.99$ N/mm, and $k_3 = -36.95$ N/mm. Note that the spring attaching B_{n+2} to ground has a negative value. This indicates that, compared to point B_n, point B_{n+2} has a lower spring constant to ground. Since k_3 is less than the sum of k_1 and k_2 the overall stiffness of the point is positive. From solid

Table 4.3.5: Gap Demonstration

	Command Signal (volts)	Sensor Signal (volts)	Bolt-to-bolt measurement (mm)	Predicted bolt-to-bolt (mm)	Apparent Gap (mm)
Calibration	-3.500	-6.986	233.76		
	-2.999	-6.035	237.16		
	-2.500	-4.945	240.82		
	-1.999	-3.970	244.17		
	-1.500	-3.001	247.40		
	-1.001	-1.960	250.75		
	-0.500	-1.036	253.80		
	0.000	-0.018	257.02		
	0.501	0.940	260.17		
	0.999	2.002	263.88		
	1.500	2.963	266.80		
	2.000	3.942	270.03		
	2.501	4.915	273.23		
	3.001	5.947	276.63		
	3.500	6.982	280.26		
Positive Gap Display					
	-2.750	-5.389	239.80	239.33	0.47
	-2.600	-5.192	240.49	239.98	0.51
	-2.500	-4.955	241.30	240.76	0.54
	-2.399	-4.750	242.11	241.44	0.67
	-2.249	-4.397	243.21	242.61	0.60
	-2.101	-4.206	243.89	243.24	0.66
	-2.001	-4.027	244.45	243.83	0.62
	-1.899	-3.716	245.57	244.85	0.71
	-1.749	-3.423	246.66	245.82	0.84
	-1.600	-3.221	247.32	246.49	0.83
	-1.501	-3.041	247.85	247.08	0.77
	-1.399	-2.743	248.74	248.06	0.68
	-1.250	-2.550	249.15	248.70	0.45
				Average	0.64
				Standard Deviation	0.13
Negative Gap Display					
	-1.099	-2.237	249.33	249.73	-0.41
	-1.000	-2.036	249.91	250.40	-0.49
	-0.999	-1.971	249.91	250.61	-0.70
	-0.979	-1.990	250.04	250.55	-0.51
	-0.900	-1.873	250.09	250.93	-0.85
	-0.750	-1.486	251.69	252.21	-0.52
	-0.600	-1.277	252.30	252.90	-0.60
	-0.500	-1.051	252.88	253.65	-0.76
	-0.400	-0.770	253.92	254.57	-0.65
	-0.250	-0.563	254.61	255.26	-0.65
	-0.101	-0.273	255.73	256.21	-0.49
	0.000	-0.052	256.26	256.94	-0.68
	0.100	0.122	256.87	257.52	-0.65
	0.250	0.450	257.84	258.60	-0.76
	0.400	0.699	258.67	259.42	-0.75
	0.501	0.922	259.64	260.16	-0.52
	0.600	1.099	260.07	260.74	-0.67
	0.749	1.402	260.96	261.74	-0.78
	0.900	1.750	262.08	262.89	-0.81
	1.000	1.902	262.59	263.39	-0.81
				Average	-0.65
				Standard Deviation	0.13

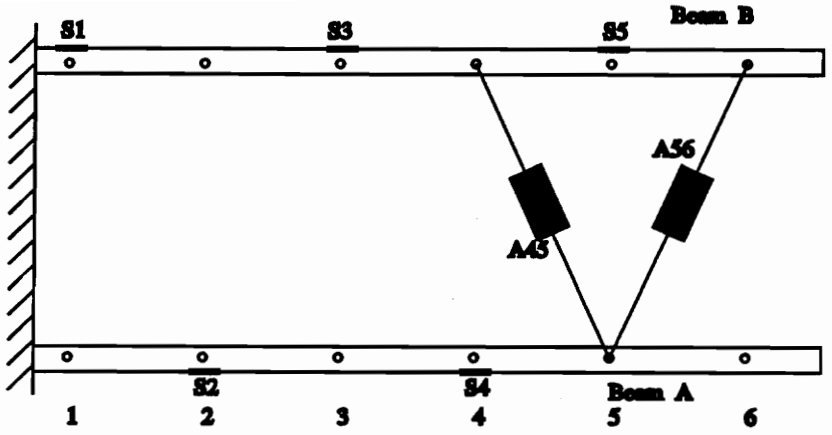

(a)

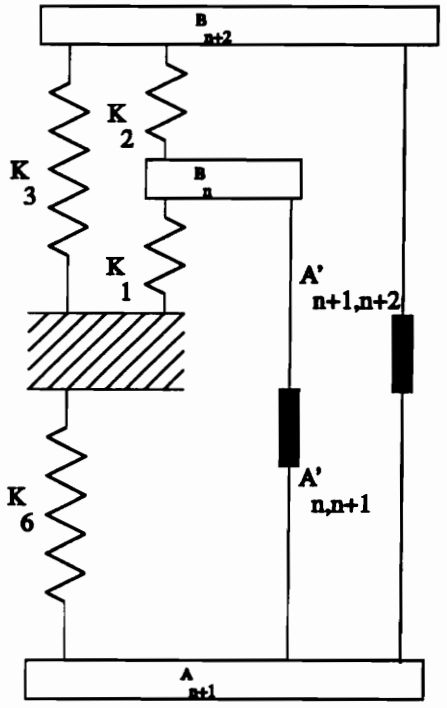

(b)

Figure 4.3.5: Two Actuator Model
a. Beam Model
b. Lumped Parameter Model

mechanics this indicates that the points further away from the fixed end have lower equivalent spring constants when compared to a point closer to the fixed end.

The experimental results are presented in Table 4.3.6. The residuals from the theory appear to have large variations since the standard deviations are 0.33 mm, 1.30 mm, and 1.12 mm for points B_4, A_5, and B_6.

Table 4.3.6: Two Actuator (A_{45} & A_{56}) Point Displacement to Actuator Extension -- Model

	B_4	A_5	B_6
Slope A_{56} (mm/mm)	0.635	0.635	1.735
Slope A_{45} (mm/mm)	-0.476	-1.576	-1.576
Average Residual(mm)	0.03	0.25	0.01
Standard Deviation of Residuals (mm)	0.32	1.30	1.11

The experimental data is then used to create a linear least squares fit as shown in Table 4.3.7. The residual standard deviation are lower but still appear to be inconclusive, in whether the model is correct, at 0.106 mm, 0.770 mm, 0.331 mm.

Table 4.3.7: Least Squares Fit of Two Actuator (A_{45} & A_{56}) Displacements to Calibrated Extension with LVDT Feedback

	B_4	A_5	B_6
Slope A_{56} (mm/mm)	0.396	0.043	0.925
Slope A_{45} (mm/mm)	-0.180	-0.694	-0.552
Average Residual (mm)	0.00	0.00	0.00
Standard Deviation of Residuals (mm)	0.11	0.77	0.33

The demonstrated gap from the single actuator case can be causing the experiment to be inconclusive to confirming the model. The effect is not only based on the individual actuator extension, but whether it is under tension or compression. This modeling is beyond the scope of this work.

4.3.3 Three Actuators with LVDT Feedback

A three actuator experiment is done with the actuators in positions A_{34}, A_{45}, and A_{56}. This allows three independent displacements to be specified and creates one additional degree of freedom. The theoretical results are tabulated in Table 4.3.8. Table 4.3.9 has the linear regression coefficients. The differences between the theoretical and measured coefficients are significant. These predictions and expected values do not allow any conclusions to be inferred. The primary reason for the discrepancy is the joint nonlinearity as discussed for the two actuator case.

Table 4.3.8: Three Actuator Point Displacement to Actuator Extension Model

	A_3	B_4	A_5	B_6
A_{34} Slope (mm/mm)	0.042	0.952	0.952	0.952
A_{45} Slope (mm/mm)	-0.454	-0.454	-1.363	-1.363
A_{56} Slope (mm/mm)	0.166	0.166	0.166	1.075
Intercept (mm)	0.000	0.000	0.000	0.000
Average Residual (mm)	0.55	0.29	0.03	1.01
Standard Deviation of Residuals (mm)	0.24	0.38	0.47	1.28

Table 4.3.9: Linear Coefficients of Fit for Three Actuator Experiment

	A_3	B_4	A_5	B_6
A_{34} Slope (mm/mm)	0.000	0.801	0.460	1.021
A_{45} Slope (mm/mm)	-0.192	-0.025	-0.650	-0.125
A_{56} Slope (mm/mm)	0.037	0.026	-0.050	0.265
Intercept (mm)	0.011	-0.008	-0.009	-0.011
Average Residual (mm)	0.00	0.00	0.00	0.00
Standard Deviation of Residuals (mm)	0.14	0.19	0.27	0.76

4.4 Strain Feedback

The system is shown to be stable and predictable for LVDT sensor feedback. It is desired to demonstrate that the position feedback apparatus, being bulky, may be replaced. The actuator extension measurements can be predicted based on the beam strain measurements as presented in Chapter 3.

The analog computer is configured together with the strain gages to produce signals proportional to the actuator lengths. These signals are then sent to the feedback input and processed. First one actuator is implemented followed by two actuators. The beam displacement, feedback signal, and the LVDT signal are recorded during the experiment. The linear coefficients for the displacement model will be examined. These experiments will demonstrate that the strain readings may replace the LVDT sensor readings.

4.4.1 One Actuator with Strain Feedback

The actuator is placed in the A_{56} position with the output of an analog computer estimating the extension. The analog computer was configured to estimate both the A_{45} and A_{56} extension. These estimations are calculated using three strain gage outputs from positions B_3, A_4, and B_5. The strain signal is found to be noisy. Therefore, since the

objective is long-term shaping, the output of the strain conditioners are filtered and then input to the analog computer. The transformation matrix between the strain voltage output and the actuator extensions can be determined as

$$\delta = E_3(AL^{-1}GH)V_\varepsilon$$

In this case the result is

$$\delta = J\begin{bmatrix} -4.472 & 4.816 & -10.00 \\ 8.600 & 6.949 & -10.00 \end{bmatrix} V_\varepsilon$$

Now that a signal proportional to the actuator extension is found as a linear combination of the strain signals, strain feedback may replace the LVDT signal.

In order to confirm that the estimate does allow the servo to respond properly, a single actuator is tested in position A_{56}. The actuator is found to respond linearly as a position servo in this case. Table 4.4.1 organizes the results of the model and the average experimental residuals for comparing the displacement model. The displacement coefficients of A_5 and B_6 in relation to the actuator extension are -0.381 and 0.718. The ratio of the slopes is 1.885, the same ratio predicted by the model.

Table 4.4.1: Point Displacement to A_{56} Actuator Extension with Strain Feedback -- Model

	A_5	B_6
Slope	-0.381 mm/mm	0.718 mm/mm
Intercept	0.00 mm	0.00 mm
Ratio of Slopes	1.885	
Residual Average	-0.19 mm	0.37 mm
Standard Deviation of Residual	0.25 mm	0.37 mm

Figure 4.4.1 shows the relation between the feedback signal from the analog computer and the LVDT sensor signal. This demonstrates that indeed strain feedback may replace the length sensor feedback, since the segments away from the zero point are linear. This demonstrates a gap since there are two groupings of LVDT calibrated extensions at a near zero feedback signal. It is noted that on each side of the gap the relation is linear. Figure 4.4.2 shows that the two point displacements are linearly related to the feedback signal from the strains.

Table 4.4.2 is a best fit of the displacements based on the calibrated extension. The correlation coefficient is 0.996 and is very good in both cases. The linear fit yields coefficients of -0.344 and 0.673 for A_5 and B_6. The 95% confidence bounds for the coefficients are presented in the table. Once again the single actuator model is confirmed as would be expected.

Table 4.4.2 Point Displacement to A_{56} Actuator Extension with Strain Feedback -- Experimental

	A_5	B_6
Slope	-0.344 mm/mm	0.673 mm/mm
95% Confidence Bounds	0.009 mm/mm	0.017 mm/mm
Intercept	-0.18 mm	0.36 mm
95% Confidence Bounds	0.05 mm	0.10 mm
Coefficient of Correlation	0.996	0.996
Ratio of slopes	1.956	
Residual Average	-0.01 mm	0.01 mm
Standard Deviation of Residual	0.13 mm	0.26 mm

The gap is still affecting the results of the calibrated extension fit, therefore Table 4.4.3 fit the displacements to the feedback signal. These fits are more accurate since the correlation coefficients are 0.999 and 1.000. Accordingly the standard deviation of the residual are lower. This shows that the point displacements are linearly related to the strain feedback signal.

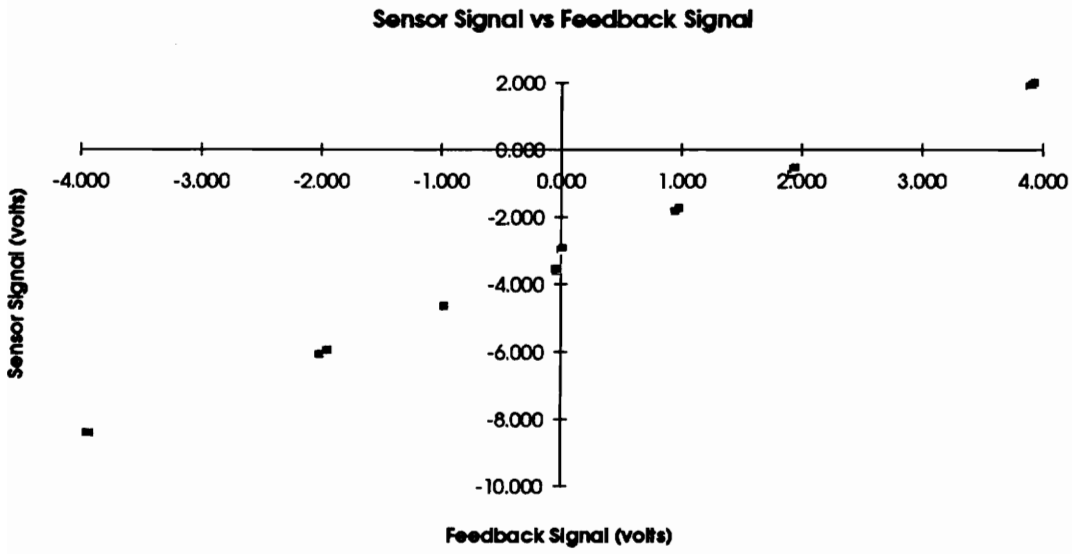

Figure 4.4.1: Linear Relation Using Strain Signals with Evident Gap

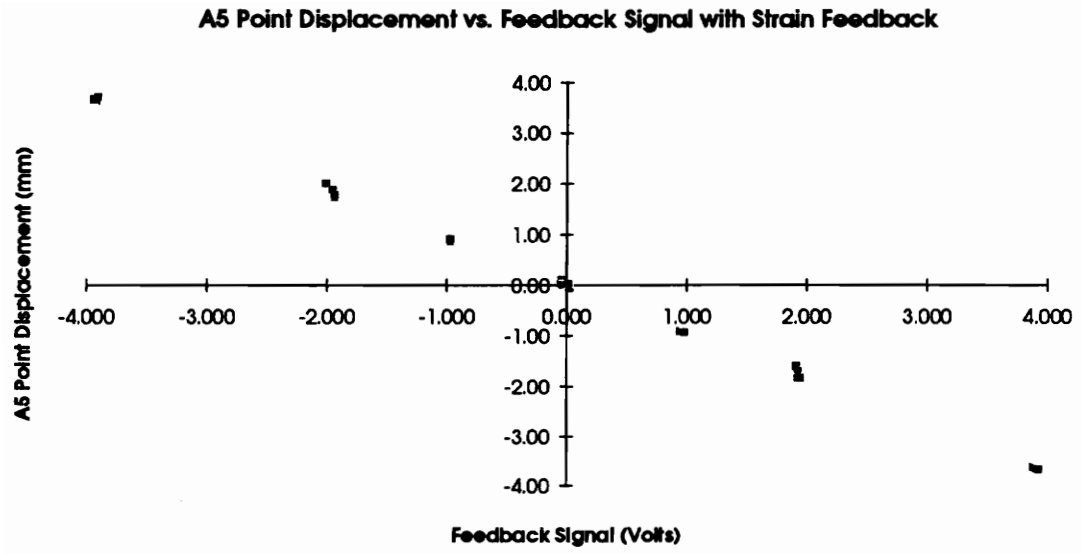

(a)

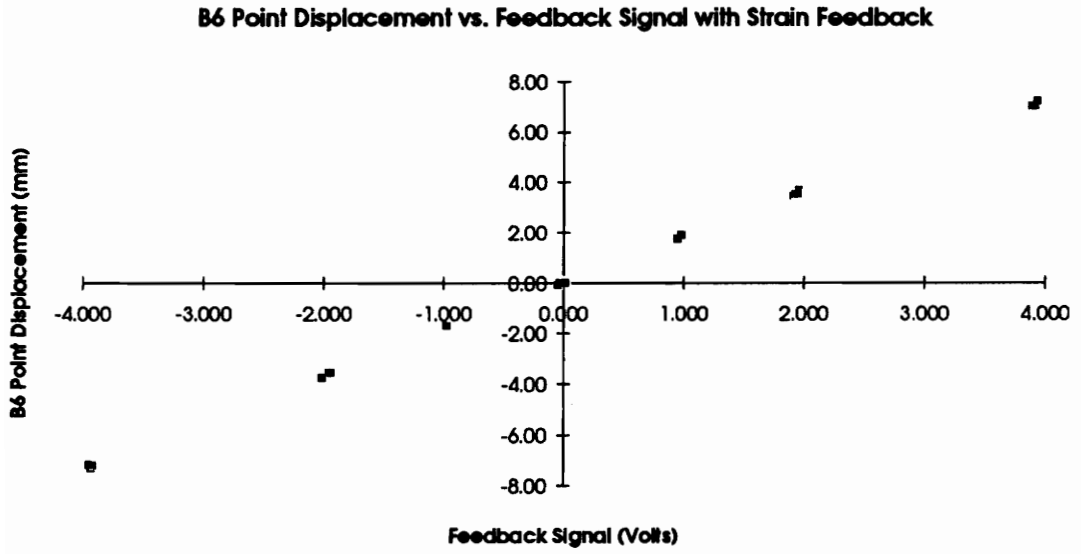

(b)

Figure 4.4.2: Linear Relation Between Point Displacement and Feedback Signal
(a) Point A_5 Displacement with Feedback Signal
(b) Point B_6 Displacement with Feedback Signal

Table 4.4.3: Point Displacement to Feedback Signal Relation -- Experimental

	A_5	B_6
Slope	-0.037 mm/mm	0.072 mm/mm
Intercept	0.01 mm	0.00 mm
Coefficient of Correlation	0.999	1.000
Ratio of Slopes	1.956	
Residual Average	0.00 mm	0.00 mm
Standard Deviation of Residual	0.06 mm	0.06 mm

The beam displacement is checked with actuator A_{56} installed. In this case, the strain feedback path is implemented. This enables a zero command voltage to result in an undeformed beam with no strain. The experimental displacements of actuator attachment points are measured by subtracting the undeformed and deformed distance between a reference wire with a micrometer. These curve fit results are tabulated on Table 4.4.4 and Table 4.4.5. A fit for the entire data set is presented as well as the positive displacements and the negative displacements data fit. These are sections fit separately because it appears to be a bilinear relationship with a gap nonlinearity. The slope of both sections are within 3% while allowing the intercept to shift.

Table 4.4.4: A_5 Displacement to LVDT Sensor Linear Fit

	Entire Data Set	Positive Displacement	Negative Displacement
Slope	-0.692	-0.744	-0.745
Intercept	-2.228	-2.602	-2.221
Coefficient of correlation	0.996	0.999	0.999

Table 4.4.5: B_6 Displacement to LVDT Sensor Linear Fit

	Entire Data Set	Negative Displacement	Positive Displacement
Slope	1.354	1.479	1.442
Intercept	4.372	5.239	4.337
Coefficient of correlation	0.996	1.000	0.999

While using the strain feedback, the LVDT sensor output is compared to the measured displacements of the points. A scatter graph of these values is shown in Fig. 4.4.3. The first notable feature of the scatter graph is that there are two groups of points for the zero displacement condition. This is noticed to arise based on the position prior to a zero command voltage. It indicates a gap nonlinearity at the joint. This arises from the joint manufacturing of the actuators. By taking the smallest difference of the LVDT sensor outputs, the gap is estimated to be 1.1 mm.

Two linear regions of the graph may be fit to check if otherwise the deformation is linear. These two independent fits result in a maximum residual of 0.11 mm. This indicates that the beam is indeed responding in a linear manner outside of the gap region.

One advantage of the strain feedback is that it is not sensitive to the joint gap and responds only based on the beam strain. Therefore the gap nonlinearity is not an issue. This occurs because rather than using the LVDT signal as a means to know the beam displacements the strain readings are used and the actuators respond to the strain rather than the LVDT signal.

4.4.2 Two Actuators with Strain Feedback

The next step is to check if two actuators acting together will function properly on the structure. The analog computer estimates are used as feedback signals. Some experimental results are tabulated in Table 4.4.6. The data reveals a slight cross-sensitivity between actuator since changing one reference signal results in movement of both actuators.

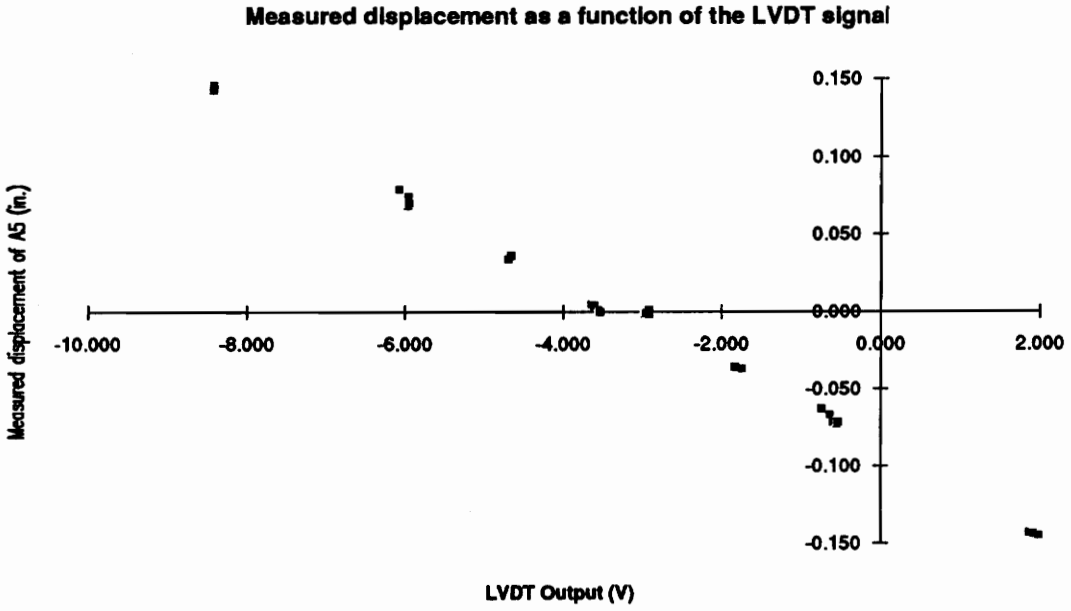

Figure 4.4.3: Beam Deflections as a Function of Sensor Output

Table 4.4.6: Theoretic Fit with Two Actuators (A_{56} & A_{45}) and Strain Feedback

	B_4	A_5	B_6
Slope A_{56} (mm/mm)	0.635	0.635	1.735
Slope A_{45} (mm/mm)	-0.476	-1.576	-1.576
Residual Average (mm)	0.63	1.57	1.69
Standard Deviation of Residual (mm)	0.48	0.97	1.42

Table 4.4.6 has the modeled linear fit values. The experiment linear fit of the displacement to the LVDT calibrated extensions is shown in Table 4.4.7. These experimental coefficient values seem to be inconclusive compared to the modeled values. This may be a direct result of the joint gap.

Table 4.4.7: Linear Fit with Two Actuators (A_{56} & A_{45}) and Strain Feedback

	B_4	A_5	B_6
Slope A_{56} (mm/mm)	0.433	0.321	1.125
Slope A_{45} (mm/mm)	-0.212	-1.083	-0.776
Residual Average (mm)	0.00	0.00	0.00
Standard Deviation of Residuals (mm)	0.17	0.37	0.39

Figures 4.4.4 and 4.4.5 depict the LVDT signal and strain calculation relationship. It shows that strain feedback is nominally linear with the LVDT signal. These graphs display how strain feedback may nominally replace LVDT feedback.

4.5 Summary

The actuator and sensor precision was established for two different feedback paths, one internal to the controller while the other was external. The test-bed experiments were performed with one, two, and three actuators. The actuator length feedback system is inherently stable and is used to confirm the displacement model. The displacement model was shown to be accurate for one actuator although the joint gap adversely affects

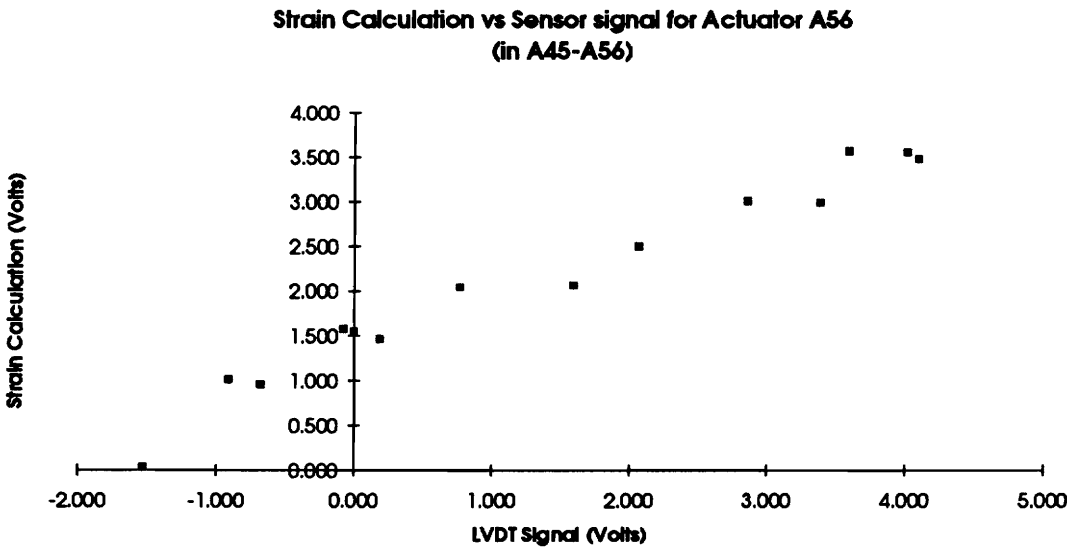

Figure 4.4.4: A_{56} Strain Calculation vs LVDT Signal

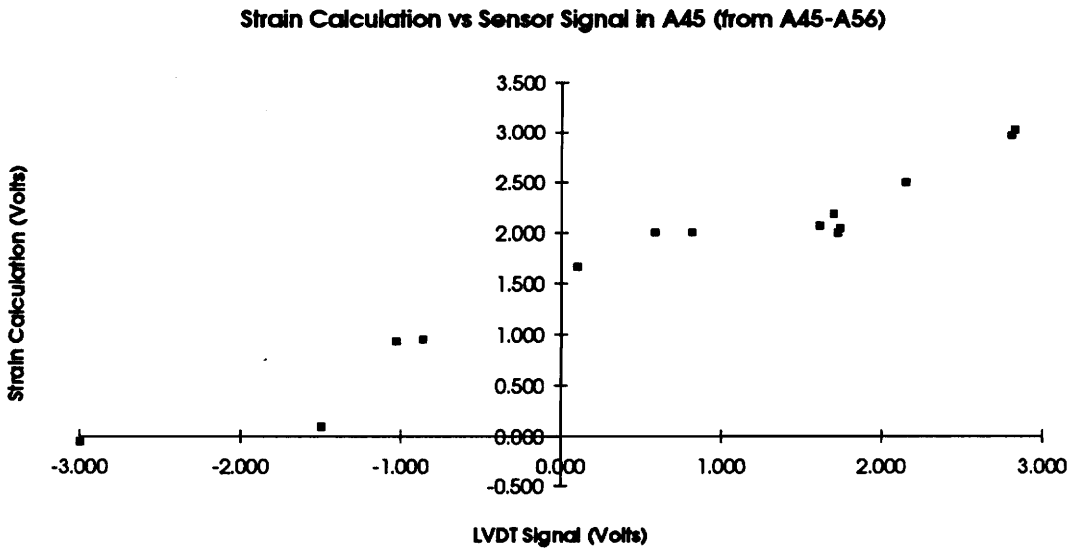

Figure 4.4.5: A_{45} Strain Calculation vs LVDT Signal

the confirmation of the multi-actuator model. The joint gap is shown clearly in Table 4.3.5.

Replacing the actuator length (LVDT) feedback with strain feedback was implemented and investigated. It was found that strain feedback may be used to control the actuator length. It was shown that strain sensors have the advantage of not being sensitive to the joint non-linearity.

Chapter 5

Conclusions & Recommendations

5.1 Conclusions

The motion of a beam system with connected active members has been experimentally demonstrated. This work demonstrates the potential for active in-flight airfoil contouring. The work involved characterization of the beam model and implementation of two control methods. Control has been provided using both length (LVDT) and strain feedback. Based on the results shown in Chapter 4 the following conclusions are drawn.

5.1.1 LVDT Feedback

It is possible to control the one actuator beam system with length feedback. The actuator works as a strict length actuator. One advantage is that the sensors and actuators are collocated and the control system is therefore always stable. The experimental results for the beam displacement conform closely with theory. The predicted and experimental ratio of spring constants were in close agreement when the actuator was in position A_{56}.

The primary drawback encountered was the manufacturing imprecision apparent by the joint gap. This causes a nonlinear response in the beam displacement. Table 4.3.5 demonstrates the gap response clearly.

The system is stable with two actuators and position feedback. This configuration, with actuators in A45 and A56, allows two degrees of freedom. The confirmation of the

system model is difficult since the joint gap results in a complex relationship which is not modeled in this work. Using three actuators, the system is stable and the individual actuators act as position servos, but the data is inconclusive in confirming the model due to the joint gap.

5.1.2 Strain Feedback

The strain signals from positions B_3, A_4, and B_5 are used to create a signal proportional to the actuator extensions A_{45} and A_{56}. Table 4.4.1 show the results. Figure 4.4.1 depicts the relation between the strain feedback and the length signal. It demonstrates the joint nonlinearity since a gap is clearly seen, yet also reveals two linear regions.

The strain signals were then used to control two actuators. A slight cross sensitivity was found since changing one reference signal results in the movement of both actuators. This could be because of the accuracy of the analog computer in calculating the correct feedback signal, due to any small perturbations in the gains.

The LVDT feedback may be replaced by the strain feedback. In fact, even with the joint gap, the strain feedback to point displacement relation is linear.

5.2 Recommendations

A few recommendations could be implemented to make to experimental results more accurate. First, the beams could be more precisely manufactured such that the joint gap is less significant for the LVDT feedback experiments. Secondly, the aluminum beams

could be replaced with a composite material which has a larger elastic displacement range. Once deformed plastically, the results with the strain feedback become inconclusive. It would also be better if the strain gages were not placed over a beam section which was machined and had a variable area moment of inertia. Finally, a digital controller could be programmed to keep the strain levels bounded to avoid plastic deformation.

References

Belyanskii, P. V. and M. I. Mustafaev, 1989. "Modal Control of the Shape of Space Structures," *Automation and Remote Control*, Vol. 49, No 8, pp. 988-995.

Bisshopp, K. E. and D. C. Drucker, 1945. "Large Deflection of Cantilever Beams," *Quarterly of Applied Math.*, Vol. 3, No. 3, pp. 272-275.

Bonnema, K. L. and W. A. Lokos, 1989. "AFTI/F-111 Mission Adaptive Wing Flight Test Instrumentation Overview," *35th International Instrumentation Symposium of Instrumentation Society of America*, Orlando, FL, April 30-Mar 4.

Bonnema, K. L. and S. B. Smith, 1988. "AFTI/F-111 Mission Adaptive Wing Flight Research Program," AIAA Technical Paper 88-2118, *Proceedings of AIAA 4th Flight Test Conference*, San Diego, CA.

Bushnell, D., 1979. "Control of Surface Configuration by Application of Concentrated Loads," *AIAA Journal*, Vol. 17, No. 1, pp. 71-77.

Bushnell, D., 1979. "Control of Surface Configuration of Nonuniformly Heated Shells," *AIAA Journal*, Vol. 17, No. 1, pp. 78-84.

Chen, G. and J. Zhou, 1990. "The Boundary Element Method for Shape Control of Distributed Parameter Elastostatic Systems," AIAA Technical Paper 90-1208-CP.

Epstein, M. and D. W. Murray, 1976. "Large Deformation In-plane Analysis of Elastic Beams," *Computers & Structures*, Vol. 6, pp. 1-9.

Frisch-Fay, R., 1962. "Large Deflections of a Cantilever Under Two Concentrated Loads," *Journal of Applied Mechanics*, March 1962, pp. 200-201.

Haftka, R. T. and H. M. Adelman, 1985. "Selection of Actuator Locations for Static Shape Control of Large Space Structures by Heuristic Integer Programming," *Computers & Structures*, Vol. 20, No. 1-3, pp. 575-582.

Haftka, R. T. and H. M. Adelman, 1985. "The Effect of Sensor and Actuator Errors on Static Shape Control for Large Space Structures," NASA TM-86446.

Hardy, R. "AFTI/F-111 Mission Adaptive Wing Technology Demonstration Program," AIAA Paper 89-10641. *Proceedings of the International Pacific Air and Apace Technology Conference*, Melbourne, Australia, Nov 13-17, 1987.

Hodges, D. H., 1984. "Proper Definition of Curvature in Nonlinear Beam Kinematics," *AIAA Journal*, Vol. 22, No. 12, pp. 1825-1827.

Kashiwase, T., M. Tabata, and K. Tsuchiya, 1991. "Shape Control of Flexible Space Structures," *Proceedings of the AAS/AIAA Spaceflight Mechanics Meeting*, Houston, TX, February 11-13, pp. 551-562.

Kuwao, F., M. Yoshihara, S. Motohashi, K. Takahara, and M. Natori, 1989. "Vibration Characteristics and Shape Control of Adaptive Planar Truss Structures," AIAA Technical Paper 89-1288-CP.

Lang, J. H., 1982. "Electrostatically Figured Membrane Reflectors: An Overview," *Large Space Antenna Systems Technology - 1982*, NASA Langley, November 30 - December 3, pp. 575-582.

Maclean, B. J., B. F. Carpenter, J. L. Draper, and M. S. Misra, 1991. "A Compliant Wing Section for Adaptive Control Surfaces," *Proceedings of the 1991 Active Materials and Adaptive Structures Conference*, Alexandria, Virginia, November 4-8, pp. 281-284.

Mettler, E., R. Scheid, and D. Eldred, 1988. "Technologies for Antenna Shape and Vibration Control," *Mobile Satellite Conference*, Pasadena, CA, May 3-5, JPL D-5260.

Padmanabhan, B., V. Arun, and C. F. Reinholtz, 1990. "Closed-form Inverse Kinematic Analysis of Variable Geometry Truss Manipulators," *Proceedings of the 1990 ASME Mechanism Conference*, DE-Vol. 26, Cams, Gears Robot and Mechanism Design, Chicago, Illinois, Sept. 16-19, pp. 99-105.

Padula, S. L., H. M. Adelman, M. C. Bailey, and R. T. Haftka. "Integrated Structural Electromagnetic Shape Control of Large Space Antenna Reflectors," *AIAA Journal*, Vol. 27, No. 6, pp. 814-819.

Rhodes, M. D. and M. M. Mikulas, Jr., 1985. "Deployable Controllable Geometry Truss Beam," NASA TM-86366.

Robertshaw, H. H. and C. F. Reinholtz, 1989. "Variable Geometry Trusses," *Smart Materials, Structures, and Mathematical Issues*. Technomic Publishing Co., Lancaster, PA, pp. 105-120.

Robertshaw, H. H., R. H. Wynn, Jr., H. F. Kung, S. L. Hendricks, W. W. Clark, 1989. "Dynamics and Control of a Spatial Active Truss Actuator," *Proceedings of the AIAA/ASME/ASCE/AHS/ASC 30th Structures, Structural Dynamics and Materials Conference*, Mobile, Alabama, April 3-5, AIAA Paper 89-1328, pp. 1473-1479.

Turner, C. D, 1991. "Design, Modeling, Analysis and Tests of Sensors and Actuators Utilized in a Mission Adaptive Wing," *Proceedings of the 1991 Active Materials and Adaptive Structures Conference*, Alexandria, VA, November 4-8, pp. 277-280.

Vita

Larry Tentor was born in Schenectady, New York on March 2, 1968. He graduated Niskayuna High in 1986, and pursued undergraduate study at the State University of New York at Buffalo. While at Buffalo he participated in the University Honors Program as well as a diversified activities schedule. In 1990 he graduate SUNY - Buffalo Summa Cum Laude and choose to pursue graduate study under Dr. Harley Cudney at Virginia Polytechnic Institute and State University. While in graduate school in turbulent economic times he first attended to research from NASA -- Langley, then choose to participate in the Southwestern Summer Sales Program, and following that he began research on this material at Grumman Aerospace. After graduation, he will participate in the Southwestern Summer Sales Program as a Field Manager and travel during the fall.

Lawrence Bernard Tentor